

NANO-ENCAPSULATION OF SILVER DOPED ZINC SULFIDE WITH INDIUM  
TIN OXIDE AND ALUMINUM DOPED ZINC OXIDE FOR FLAT PANEL DISPLAY  
APPLICATIONS

By  
MICHAEL OLLINGER

A DISSERTATION PRESENTED TO THE GRADUATE SCHOOL  
OF THE UNIVERSITY OF FLORIDA IN PARTIAL FULFILLMENT  
OF THE REQUIREMENTS FOR THE DEGREE OF  
DOCTOR OF PHILOSOPHY

UNIVERSITY OF FLORIDA

2002

LD

1780

2002

,051

This work is dedicated to my parents. Their continual support made it possible for me to complete this work.

## ACKNOWLEDGMENTS

First, I would like to thank my advisor and mentor, Dr. Singh for his advice, support, and the freedom to pursue my own research during my years at the University of Florida. Without his encouragement and drive, I may have never graduated. I was very fortunate to have had the opportunity to work for him.

I would also like to thank all of my fellow group members, past and present. They were always willing to lend a hand when I needed it. They also made my stay here in Gainesville very enjoyable. Finally, I would like to thank all of my friends and family, as they were very patient and supportive during my stay at UF.

## TABLE OF CONTENTS

	<u>page</u>
ACKNOWLEDGMENTS .....	iii
LIST OF TABLES .....	vi
LIST OF FIGURES .....	vii
ABSTRACT .....	xi
 CHAPTER	
1 INTRODUCTION .....	1
2 LITERATURE REVIEW .....	3
Field Emission Displays .....	4
Cathodoluminescence .....	6
Electron Beam – Solid Interactions .....	7
Photon Generation.....	10
Configurational Coordinate Model.....	11
Luminescent Transitions.....	13
Cathodoluminescent Degradation.....	14
Electron Beam Stimulated Surface Chemical Reactions .....	15
Carbon Accumulation .....	21
Point Defects .....	22
Charging.....	23
Transparent Conducting Oxides .....	24
Background/History .....	24
Optical Properties.....	26
Electrical Properties .....	31
3 EXPERIMENTAL PROCEDURES .....	51
Introduction.....	51
Sample Preparation .....	51
ZnS:Ag .....	51
Coating Process .....	51
Experimental Characterization Techniques .....	53
Cathodoluminescent Degradation Measurements.....	53
Scanning Electron Microscopy .....	55

Energy-Dispersive X-Ray Spectroscopy.....	56
Auger Electron Spectroscopy.....	56
X-Ray Photoelectron Spectroscopy .....	58
Residual Gas Analysis.....	59
Four Point Probe .....	60
UV-VIS .....	60
 4 EFFECT OF ITO COATINGS ON ZnS:Ag ON CL DEGRADATION.....	 71
Introduction.....	71
Background .....	71
Results and Discussion .....	72
Indium Tin Oxide – Coated ZnS:Ag.....	72
Effect of the Partial Pressure of Water on CL Degradation.....	75
 5 EFFECT OF OXYGEN PARTIAL PRESSURE DURING ZAO GROWTH ON CL DEGRADATION OF ZnS:Ag .....	 85
 6 CONCLUSIONS.....	 109
 LIST OF REFERENCES .....	 112
 BIOGRAPHICAL SKETCH .....	 116

## LIST OF TABLES

<u>Table</u>	<u>page</u>
5-1    This table lists the ZAO film thickness, ZAO film resistivity, and ZAO transmittance at 100 mTorr, 0.6 mTorr, and 0.14 mTorr.....	86
5-2    This table lists the growth rate of ZAO at 100 mTorr, 0.6 mTorr, and 0.14 mTorr. .86	86
5-3    This table lists the Zn 2p peak values before and after CL degradation.....	88

## LIST OF FIGURES

<u>Figure</u>	<u>page</u>
2-1 Schematic of a typical field emission display.....	34
2-2 Comparison between different models for stopping power. ....	35
2-3 A schematic illustration showing the increase in interaction volume with the increase in electron beam energy.....	36
2-4 Schematic energy level scheme of the luminescent ion A. R – radiative return; NR – nonradiative return to the ground state.....	37
2-5 Configurational coordinate model of a luminescent center. ....	38
2-6 Schematic diagram of luminescence transitions between the conduction band ( $E_C$ ), the valence band ( $E_V$ ), and exciton ( $E_E$ ), donor ( $E_D$ ), and acceptor ( $E_A$ ) levels in the luminescent material.....	39
2-7 Auger spectra before and after electron beam aging of the ZnS phosphor.....	39
2-8 Semilogarithmic plot of normalized CL intensity vs. dose for P22B ZnS:Ag phosphor irradiated with 2 keV electrons in residual vacuum at pressures between $6 \cdot 10^{-9}$ and $7 \cdot 10^{-8}$ Torr. ....	40
2-9 Sulfur Auger electron peak height vs. dose of 2 keV electrons from P22B ZnS:Ag phosphor at residual vacuum pressures between $7 \cdot 10^{-9}$ and $7 \cdot 10^{-8}$ Torr. (a) Linear plot; (b) semilogarithmic plot. ....	41
2-10 CL intensity vs. sulfur Auger electron beam peak height for ZnS:Mn thin films in $1 \cdot 10^{-6}$ Torr $O_2$ irradiated by 4 keV electrons. Note the linear relationship, however, extrapolation of the plot towards zero will result in an intercept at zero on the Auger peak height axis before the zero is reached on the CL intensity axis. ....	42
2-11 Plot of $O_2$ pressure vs. the time to result in a 50% decrease of the sulfur Auger peak height for ZnS:Mn irradiated with 2 keV electrons. Note the linear dependence upon pressure. ....	43
2-12 CL intensity vs. electron dose from ZnS:Mn in $1 \cdot 10^{-6}$ Torr $O_2$ for 1, 2, 4 keV primary beam electrons.....	44



2-13	Thermoluminescent intensity vs. temperature (glow curves) of ZnS:Mn sample before and after degradation to $\sim 160 \text{ C/cm}^2$ in $1 \cdot 10^{-6}$ Torr $\text{O}_2$ with 4 keV electrons. ....	45
2-14	Charging effect on the CL intensity. ....	46
2-15	The electron band diagram of a semiconductor which surface is negatively charged. ....	47
2-16	Illustration of the Burstein-Moss shift, which increases the optical band gap due to occupancy of states in the conduction band. ....	48
2-17	Schematic frequency dependence of an alkali metal according to the free electron theory without damping. $\nu_1$ is the plasma frequency. ....	49
2-18	Theoretical plots of relationships between electrical and optical properties for (a) reflectance versus carrier concentration, (b) absorptance versus carrier concentration, and (c) absorptance versus carrier mobility. ....	50
3-1	A schematic of the modified pulsed laser deposition used for particle coatings. ....	62
3-2	Picture of mechanical shaker used for particle fluidization. (a) Picture of side view of the mechanical shaker and (b) Picture of top view of the mechanical shaker. ....	63
3-3	Schematic illustration of the CL measurement system for degradation experiments. ....	64
3-4	Schematic illustration of CL system used in conjunction with a JEOL 6400 SEM. ....	65
3-5	A schematic illustration showing a cross-sectional view of a typical SEM electron column, deflection system, and electron detectors. ....	66
3-6	Energy level diagram of solid Si, including the density of states of the valence and conduction bands, a schematic representation of the Si $\text{KL}_{2,3}\text{L}_{2,3}$ Auger transitions, and a subsequent LVV Auger transition [Bru92]. ....	67
3-7	These figures show two different forms of the secondary electron energy spectra from a slightly contaminated Fe surface. (a). Shows the directly acquired data, and (b) shows a subsequently mathematically derived spectra that allows for improved signal-to-noise ratio in the raw data. ....	68
3-8	Schematic representation of the electronic energy levels of a carbon atom and the photoionization of a carbon 1s electron. ....	69
3-9	Shows a schematic of a residual gas analyzer. It is comprised of an ion source, a quadrupole separation system and an ion detector. ....	69

3-10	Schematic setup of a four-point probe method for measuring sheet resistance.....	70
4-1	Auger electron spectroscopy spectra of indium tin oxide coated ZnS:Ag. (a) AES spectra of $\sim 1 \mu\text{m}$ area. (b) AES spectra of $\sim 100 \mu\text{m}$ area.....	78
4-2	Cathodoluminescence degradation curves for commercial ZnS:Ag and ZnS:Ag coated with indium tin oxide at $6.1 \times 10^{-7}$ Torr.....	79
4-3	X-ray photoelectron spectroscopy results of the Zn $2p_{3/2}$ peak for (a) the commercial ZnS:Ag powder, (b) the electron beam irradiated ZnS:Ag sample coated with indium tin oxide, and (c) the electron beam irradiated uncoated ZnS:Ag powder.....	80
4-4	X-ray photoelectron spectroscopy results of the S $2p$ peak for (a) the commercial ZnS:Ag powder, (b) the electron beam irradiated ZnS:Ag sample coated with indium tin oxide, and (c) the electron beam irradiated uncoated ZnS:Ag powder....	81
4-5	RGA spectra of the high and low water partial pressures used during CL degradation.....	82
4-6	Cathodoluminescence degradation curves for commercial ZnS:Ag and ZnS:Ag coated with indium tin oxide at $1 \times 10^{-7}$ Torr.....	83
4-7	CL spectra comparison of coated and uncoated ZnS:Ag.....	84
5-1	This figure shows the optical spectra of ZAO deposited on Si at UV-VIS data of ZAO films grown at 100 mTorr, 0.6 mTorr, and 0.14 mTorr.....	93
5-2	This figure shows the CL degradation curves of ZnS:Ag coated with ZAO at oxygen deposition pressures 100 mTorr, 0.6 mTorr, and 0.14 mTorr.....	94
5-3	XPS results of Zn $2p$ peak of ZAO thin films deposited on silicon wafers at 100 mTorr, 0.6 mTorr, and 0.14 mTorr before and after degradation.....	95
5-4	RGA spectra taken during CL degradation experiments of ZnS:Ag coated with ZAO at 100 mTorr, 0.6 mTorr, and 0.14 mTorr.....	96
5-5	TEM micrographs of ZnS:Ag particles coated with ZAO. (a). TEM micrograph showing ZAO coating on ZnS:Ag at a oxygen deposition pressure of 0.6 mTorr. (b). TEM micrograph showing ZAO coating on ZnS:Ag at a oxygen deposition pressure of 0.6 mTorr.....	97
5-6	TEM micrographs of ZnS:Ag particles coated with ZAO. (a). TEM micrograph showing ZAO coating on ZnS:Ag at a oxygen deposition pressure of 0.6 mTorr. (b). TEM micrograph showing ZAO coating on ZnS:Ag at a oxygen deposition pressure of 0.6 mTorr.....	98

5-7	Micrographs of uncoated ZnS:Ag before degradation. (a) SEM micrograph of ZnS:Ag before degradation. (b) CL micrograph of ZnS:Ag before degradation. ....	99
5-8	Micrographs of uncoated ZnS:Ag after degradation. (a) SEM micrograph of ZnS:Ag after degradation. (b) CL micrograph of ZnS:Ag after degradation. ....	100
5-9	Micrographs of ZnS:Ag coated with ZAO at 100 mTorr before degradation. (a) SEM micrograph of ZnS:Ag coated with ZAO before degradation. (b) CL micrograph of ZnS:Ag coated with ZAO before degradation. ....	101
5-10	Micrographs of ZnS:Ag coated with ZAO at 100 mTorr after degradation. (a) SEM micrograph of ZnS:Ag coated with ZAO after degradation. (b) CL micrograph of ZnS:Ag coated with ZAO after degradation. ....	102
5-11	Micrographs of ZnS:Ag coated with ZAO at 0.6 mTorr before degradation. (a) SEM micrograph of ZnS:Ag coated with ZAO before degradation. (b) CL micrograph of ZnS:Ag coated with ZAO before degradation. ....	103
5-12	Micrographs of ZnS:Ag coated with ZAO at 0.6 mTorr after degradation. (a) SEM micrograph of ZnS:Ag coated with ZAO after degradation. (b) CL micrograph of ZnS:Ag coated with ZAO after degradation. ....	104
5-13	Micrographs of ZnS:Ag coated with ZAO at 0.14 mTorr before degradation. (a) SEM micrograph of ZnS:Ag coated with ZAO before degradation. (b) CL micrograph of ZnS:Ag coated with ZAO before degradation. ....	105
5-14	Micrographs of ZnS:Ag coated with ZAO at 0.14 mTorr after degradation. (a) SEM micrograph of ZnS:Ag coated with ZAO after degradation. (b) CL micrograph of ZnS:Ag coated with ZAO after degradation. ....	106
5-15	Micrographs of ZnS:Ag coated with ZAO at 0.6 mTorr showing the degraded region after degradation. (a) SEM micrograph of ZnS:Ag coated with ZAO after degradation. (b) CL micrograph of ZnS:Ag coated with ZAO after degradation. ....	107
5-16	SEM micrographs of ZAO thin film deposited on silicon wafer at an oxygen pressure of 0.14 mTorr. (a) Shows the ZAO thin film before degradation and (b) shows the variation between the degraded and non-degraded area. ....	108

Abstract of Dissertation Presented to the Graduate School  
of the University of Florida in Partial Fulfillment of the  
Requirements for the Degree of Doctor of Philosophy

NANO-ENCAPSULATION OF SILVER DOPED ZINC SULFIDE WITH INDIUM  
TIN OXIDE AND ALUMINUM DOPED ZINC OXIDE FOR FLAT PANEL DISPLAY  
APPLICATIONS,

By

Michael Ollinger

December 2002

Chair: Dr. Rajiv Singh

Major Department: Materials Science and Engineering

Reduction in cathodoluminescent degradation through the application of nano-meter thick films of indium tin oxide (ITO) and aluminum doped zinc oxide (ZAO) has been investigated using x-ray photoelectron spectroscopy (XPS), cathodoluminescent degradation, scanning electron microscopy, transmission electron spectroscopy, and optical spectrometry. The partial pressure of water and the oxygen deposition pressure used during the coating process were controlled as parameters critical to degradation. The cathodoluminescent measurements were performed at vacuum levels between  $1 \cdot 10^{-7}$  to  $5 \cdot 10^{-5}$  Torr as measured by residual gas analysis. The primary electron beam used in the degradation experiments varied from 5-15 keV and the electron current density varied between two conditions:  $10 \mu\text{A}/\text{cm}^2$  and  $0.10 \mu\text{A}/\text{cm}^2$ . The ITO coatings were deposited at  $1 \cdot 10^{-5}$  Torr while the ZAO films were deposited at 100 mTorr, 0.6 mTorr, and 0.14 mTorr using a modified pulsed laser ablation technique.

For the ITO coated ZnS:Ag phosphors, the amount of water vapor pressure present during cathodoluminescent degradation had a dramatic effect on the brightness lifetime. The higher the partial pressure of water, the faster the degradation rate of the phosphor. The ITO coating on the ZnS:Ag phosphor reduced the rate of cathodoluminescent degradation at both partial pressures of water that were studied. XPS showed that the coatings provided sufficient protection against the adverse affects from the water vapor.

For the ZAO coated ZnS:Ag phosphors, it was shown that the partial pressure used during the coating process effected the cathodoluminescent degradation lifetimes. The coating performed at the lowest vacuum level of oxygen provided the longest brightness lifetime. This increased phosphor lifetime was attributed to the highly deficient nature of the ZAO coating at this vacuum pressure and the continuous nature of the coating. XPS showed that the ZAO deposited at lower oxygen pressures showed a higher degree of oxidation than the other two cases. Indicating that the ZAO coating was able to behave as a sacrificial layer, which was attacked by the reactive atomic oxygen, created from the electron beam stimulated surface chemical reactions. The TEM results showed that the lower the deposition pressure, the better the coverage of the coatings. The improved conformal coverage provides better protection of the phosphor surface from the harmful residual gases, which led to improved CL degradation lifetimes.

## CHAPTER 1 INTRODUCTION

For more than thirty years, the display industry has attempted to create a thin, flat, low power version of the highly successful cathode ray tube (CRT). While efforts have led to a number of flat panel display (FPD) technologies, not one including the active matrix liquid crystal display (AMLCD), the present market leader in FPDs, has met all of the needs for reduced power consumption, brightness efficiency, video response, viewing angle, operating temperature, full color gamut and scalability [Can02].

In contrast, field emission display (FED) technology meets all these requirements, but its reliability has been plagued by technological shortcomings. These can be grouped into four problem areas: phosphor screens, emitter tips and emitter tip arrays, vacuum requirements, and FED packaging. This research will focus on the problems associated with the phosphor screens.

Since the CRT and FED share a common trait, the use of a directed, accelerated electron beam to induce cathodoluminescence (CL), the FED has adopted the sulfide-based phosphors that are used in CRTs. However, the use of these sulfide-based phosphors in FEDs has resulted in a rapid decay of screen brightness during continuous electron beam bombardment. The mechanisms of this brightness loss as well as fundamental background to cathodoluminescence are reviewed in Chapter 2. Chapter 3 presents the experimental sample preparation and methods of characterization. Chapter 4 presents the results and discussion of the effects of coating ZnS:Ag with indium tin oxide while Chapter 5 presents the results and discussion of the effects of oxygen deposition

pressure during aluminum-doped zinc oxide growth on ZnS:Ag has on cathodoluminescent degradation lifetimes. Finally, Chapter 6 contains the conclusions of this work.

## CHAPTER 2 LITERATURE REVIEW

Since the invention and commercial introduction of the cathode ray tube (CRT) over 100 years ago (1897), the CRT has dominated the visual display market [Kel97]. Not until recently, with the demand for smaller, lighter, more portable, and less power consuming displays, have new technologies been developed. These new demands have led to the development of a variety of new technologies: liquid crystal display (LCD), plasma display panel (PDP), active matrix liquid crystal display (AMLCD), thin film electroluminescent device (TFEL), and field emission display (FED). Currently, the AMLCD dominates the portable computer and hand held computer markets while the PDP is leading market sales in large viewing area flat panel displays [Reu00]. However, the AMLCD has many limitations in the areas of viewing angle, temperature range, power consumption, smearing of fast moving video images, and cost [Cat95]. While the PDPs are trying to reduce their power consumption and cost [Reu00], FEDs, which are currently being produced on a prototype basis, are believed to have the brightest future in the flat panel display industry [Reu00, Tro96, Hol99]. These displays exhibit wide viewing angles, fast response times, wide operating temperature range, high durability, and low power consumption [Hol96]. Even though FEDs possess many properties desirable for FPDs, they have reliability issues associated with phosphor lifetimes, emitter tip and emitter tip array reliability, packaging, as well as meeting vacuum requirements.



## Field Emission Displays

Field emission displays work on the same principles as standard picture tubes used by desktop computers and televisions. In both displays, electrons are directed onto a phosphor screen to produce a viewable picture. Since CRTs and FEDs operate on similar principles, FEDs have adopted the use of the same sulfide-based phosphors. Sulfide-based phosphors possess the highest luminous efficiencies among all phosphors available on the market, which is the reason they have been applied to FEDs [Hol99]. The typical red, blue, and green phosphors used in CRTs are  $\text{Y}_2\text{O}_2\text{S}:\text{Eu}$ ,  $\text{ZnS}:\text{Ag}$ , and  $\text{ZnS}:\text{Cu}, \text{Cl}, \text{Al}$  respectively. One vital difference between the two display types is that FEDs use millions of sharp emitter tips to excite the phosphors, while CRTs use three electron guns (one for each color). By using thousands of individual electron sources behind each pixel, the side profile of the display can be drastically reduced since the emitters can now be placed in close proximity to the phosphor screen without having to worry about a high temperature thermionic source causing damage to the phosphor screen. Figure 2-1 shows a schematic of a typical FED setup.

As shown in Figure 2-1, the electron beam is generated at the emitter tips and is directed to the phosphors on the faceplate, which are excited to produce the luminescence that is seen by the viewer. These emitter tips are part of an emitter tip array that contains millions of emitter tips. At each column/row junction, there are as many as 4,500 emitters [Can02]. Then by applying a small voltage across the row cathode and the column gate, electrons are emitted from these nano-tips. This process of field emission has been accurately described by the Fowler-Nordheim (FN) equation:

$$J = \left[ A \cdot \frac{(\beta \cdot V)^2}{\Phi} \right] \cdot e^{-\left[ \frac{B \Phi^{\frac{1}{2}}}{\beta V} \right]} \quad (2-1)$$

where  $J$  is the current density,  $V$  is the applied voltage,  $\Phi$  is the work function,  $A$  is a function of  $\Phi$ ,  $B$  is a constant and  $\beta$  is a geometrical factor dependent on the electrode configuration such that  $F = \beta V$ , where  $F$  is the magnitude of the electric field at the emitting surface. The important thing to notice from this equation is that the electron emission current depends exponentially on the electronic state (as modified by adsorbed gas species), the geometry of the emitting surface and the electrodes of the system through  $\Phi$  and  $\beta$ , respectively [Sch95].

Currently, field emitter arrays (FEAs) using a Spindt structure [Spi76] of molybdenum or silicon [Reu00] are being pursued for commercialization in FEDs. Even though Mo and Si FEAs are the most commonly used emitter tip materials, they still do not meet all the demands needed in FEDs. These emitter tips have been found to be extremely sensitive to the presence of oxygen containing gases in the vacuum envelop. The primary source of residual gas contamination arises from electron-beam desorption of phosphors, outgassing due to high temperature processing and diffusion through the package [Gil00].

The two primary methods by which the residual gases degrade the electron emission of the emitter tips are by electron beam dissociation of the adsorbed oxygen containing species on the emitter tips [Wei98, Gil00, Ito93] and ionization of the residual gases, which in turn causes sputtering of the emitter tip [Gil00, Sch95]. Wei et al. [Wei98] showed that the dissociation of the residual gases mainly occurred near the apex of the emitter tip by using x-ray photoelectron spectroscopy to detect oxidized Mo. This oxidation was shown to increase the work function of the emitter tip and thus reduce the

amount of electron emission. Ion bombardment of the emitter tip surface occurs primarily because of the formation of ions by the collision of energetic field-emitted electrons with neutral gas molecules in the interelectrode vacuum gap between the cathode and the anode. The resultant surface roughening and sputtering typically leads to a gradual increase in the magnitude of the emission current and fluctuations in the current at a constant applied voltage. If unchecked, this process terminates with a vacuum arc and destruction of the cathode [Sch95].

Once the electrons overcome the barrier height of the material and tunnel through the surface barrier, they are accelerated across the anode-cathode gap and strike the phosphor screen. This acceleration occurs due to a positive potential ( $<1$  keV for low voltage phosphors or 5-10 keV for high voltage phosphors) applied to the transparent electrode between the phosphor screen and faceplate. When the electrons strike the phosphors, they become excited and emit luminescence upon relaxation, which is seen by the viewer.

### **Cathodoluminescence**

When some materials are impacted with certain forms of energy, they will emit photons in excess of thermal radiation. This process is known as luminescence, and it can be categorized based on the type of excitation source. These categories include photoluminescence, cathodoluminescence, electroluminescence, triboluminescence, X-ray luminescence, and chemiluminescence, among others [Has90]. Photoluminescence is the excitation by photons, typically a UV lamp. Cathodoluminescence refers to the excitation by a beam of energetic electrons. Electroluminescence occurs when a voltage is applied across some materials creating an electric field to produce the excitation. Triboluminescence is a result of mechanical energy, such as grinding. X-ray

luminescence is produced as a result of X-ray bombardment. Finally, chemiluminescence is due to energy imparted to the material from chemical reactions [Bla94].

In addition to classifying the various types of luminescence by their excitation source, they are further distinguished by the length of the delay time between the excited and relaxed states. These two different regimes are referred to as fluorescence and phosphorescence. The critical photon emission time that separates these two regimes is  $10^{-8}$  seconds after excitation with materials having excitation occur within the initial  $10^{-8}$  seconds termed fluorescent materials and those with longer emission lifetime's phosphorescent materials. These phosphorescent materials are called phosphors [Bla94].

#### **Electron Beam – Solid Interactions**

When an electron beam strikes the surface of a material, the electrons can interact with the atoms in the material and undergo two types of collisions: elastic or inelastic. In an elastic collision, the electron interacts with the nucleus of the atom and is deflected with little to no energy loss. If the electron is deflected away from the surface of the material, it is known as a backscattered electron. However, in an inelastic collision, the incident electron interacts with the electrons of the atoms in the material and imparts some of the incident electron's energy to the atom. The atom is now in an excited state. When the atom returns to the ground state, it can produce Auger electrons, X-rays, secondary electrons, photons, and phonons [Has90, Yac90]. In this research, the focus will be on the production of photons.

As the electron travels into the material, it loses some of its energy with each inelastic collision. The amount of incremental energy ( $dE$ ) that the electron loses over a

distance of travel (ds) due to an inelastic collision can be found from the Bethe equation [Has90, Yac90, Gre01]:

$$\frac{dE}{ds} = -\frac{785 \cdot \rho \cdot Z}{A \cdot E} \cdot \ln\left(\frac{1.166 \cdot E}{J}\right) \quad (2.2)$$

where A is the atomic weight in g/mol, Z is the atomic number, E is the electron energy,  $\rho$  is the density in g/cm<sup>3</sup>, and J is the mean ionization potential in eV. The latter is the average energy loss per interaction (for all possible energy loss processes), and it can be expressed as

$$J = 9.76 \cdot Z + \frac{58.5}{Z^{0.19}} \quad (\text{eV}) \text{ for } Z \geq 13 \quad (2.3)$$

$$J = 11.5 \cdot Z \quad (\text{eV}) \text{ for } Z \leq 12 \quad (2.4)$$

The Bethe equation works well in the energy range where  $E \gg J$ , but as E approaches J, the stopping power rises to a maximum at  $E \approx 2.5J$  and then drops quickly to zero at  $E = J/1.166$ , since the function becomes dominated by the logarithmic term [Joy89]. Thus, the Bethe equation has gone through a series of modifications. Rao-Sahib and Wittry [Rao74] made the first major adjustments allowing for the energy range to extend to voltages as low as 500 V:

$$\frac{dE}{ds} = -\frac{785 \cdot \rho \cdot Z}{1.2588 \cdot A \cdot \sqrt{E \cdot J}} \quad \text{for } E < 6.34 J \quad (2.5)$$

Joy and Luo [Joy89] further modified this equation since the Rao-Sahib and Wittry expression overestimates the stopping power by more than a factor of two. This causes related factors such as electron range, secondary electron, and x-ray yields to become erroneous. Figure 2-2 shows a comparison of the stopping power in copper for the Bethe expression, the Rao-Sahib and Wittry expression, and data from an electron gas model of

Tung et al. Joy and Luo changed the quantity  $J$  and made it energy dependent rather than just a constant:

$$J' = \frac{J}{1 + k \left( \frac{J}{E} \right)} \quad (2.6)$$

where  $J'$  is the new mean ionization potential,  $J$  is still the average energy loss per interaction, and  $k$  is a fitting parameter. The constant  $k$  is a materials dependent variable that varies from 0.7 to 0.9, but is usually around 0.85 [Rao74, Joy89, Gre01].

The stopping power equations above provided an indication of how electrons lose energy in a solid, but they did not give an accurate indication of the interaction volume. Some of the electrons from the incident beam will undergo elastic collisions (no energy loss) in the solid and are redirected. Then equation 2.1 can be integrated to find the length of an individual electron's trajectory. This is known as the Bethe range. However, the interaction volume will be much smaller due to scattering. The interaction volume is known as the Gruen, electron beam, or penetration range and expresses as

$$R_e = \left( \frac{k'}{\rho} \right) E_0^\alpha \quad (2.7)$$

where  $\rho$  is the density,  $E_0$  is the electron beam energy,  $k'$  depends on the atomic number and is a function of energy, and  $\alpha$  depends on the atomic number and  $E$  [Yac90].

Various equations have been given for the solution to this problem, but the one most widely accepted was proposed by Kanaya and Okayama:

$$R_e = \left( \frac{0.0276 \cdot A}{\rho \cdot Z^{0.889}} \right) E_0^{1.67} \text{ (}\mu\text{m)} \quad (2.8)$$

where  $E_0$  is in keV,  $A$  is in g/mol,  $\rho$  is in g/cm<sup>3</sup>, and  $Z$  is the atomic number [Yac90]. As shown in Figure 2-3, this equation shows how the interaction volume increases as the incident electron beam energy increases.

As the incident electron travels through the lattice, it can have multiple interactions with the nuclei and/or the electrons of atoms in the lattice. Therefore, one electron can generate a number of secondary electrons. The number of electron-hole pairs generated per incident electron is known as the generation factor and can be expressed as

$$G = \frac{E(1-\gamma)}{E_i} \quad (2.9)$$

where  $\gamma$  represents the fractional electron beam energy lost due to backscattered electrons.  $E_i$  is the ionization energy, the energy needed to form a single electron-hole pair. The ionization energy is related to the bandgap of the material by

$$E_i = 2.8 \cdot E_g + M \quad (2.10)$$

where  $M$  is between 0 and 1 eV, depending on the material in question [Yac90].

### Photon Generation

Once the incident electron has transferred its energy to the solid, this energy can be used to produce visible light. However, not all instances of electron energy transfer result in the emission of visible light. In addition to the luminescence process, there is a competing nonradiative process.

In the luminescence process, some of the energy of the incident electron is absorbed by a luminescent center, called an activator, raising it to an excited state (Figure 2-4). When the excited state returns to the ground state through the recombination of an

electron and a hole, it does so by the emission of a photon. This is known as a radiative transition. When the atom relaxes without emission of a photon, it is called a nonradiative transition. In this case, the energy from the excited state is used to excite the vibrations of the host lattice (to heat the lattice). Therefore, in order to create efficient luminescent materials it is necessary to suppress this nonradiative process [Has90, Bla94].

When an electron and a hole radiatively recombine, the emitted photon will be characteristic of the energy levels involved, which is determined by the electronic states of the activator. The photon energy ( $h\nu$ ) is given by

$$h\nu = E_f - E_i \quad (2.11)$$

where  $E_f$  and  $E_i$  are the energy of the final and initial states, respectively. This photon energy is frequently referred to by its wavelength instead of electron-volts. The equation, which relates the two units, is

$$\lambda \cong \frac{1.2398}{E} \quad (2.12)$$

where  $E$  is the photon energy in eV and  $\lambda$  is in  $\mu\text{m}$  [Bru92, Yac90].

### Configurational Coordinate Model

To explain the shape of an optical absorption band, the conditions for photon emission, the conditions for nonradiative return to the ground state, and lattice vibrations, the configurational coordinate model Figure 2-5 is used [Bla94, Has90, Yac90]. This diagram describes the luminescent center's excitation process as well as the subsequent photon emission or nonradiative return to the ground state. In Figure 2-5, the x-axis is the deviation from the ion equilibrium distance (i.e., the configurational coordinate) and the y-axis represents the potential energy for the ground and excited states. Also, the



curves  $E_g$  and  $E_e$  in Figure 2-5 represent the energies of a luminescent center in the ground state and in the excited state, respectively. Since the stable (equilibrium) configuration of the interacting atoms will be different for both states, the minima of the two curves do not correspond. When an incident electron excites the luminescent center, it is represented by a vertical transition from the stable ground state, point O on  $E_g$ , to point B on  $E_e$  [Bla94, Has90]. This transition is shown in Figure 2-5 as a vertical jump because of the Franck-Condon principle. The principle states that the electronic state transition time is much shorter ( $10^{-16}$  s) than the vibrational period of the neighboring nuclei ( $10^{-13}$  s). Thus, the electronic transitions are said to occur in static surroundings causing the absorption and emission transitions to be vertical [Yac90]. Immediately after this electronic transition to the excited state, a new equilibrium is reached by changing its atomic configuration from B to the new equilibrium, A, along the curve  $E_e$ , with the excess energy dissipated as heat. After some period of time (the life of the luminescent center), the excited state relaxes back to the ground state by a radiative transition from A to D, emitting the energy difference between the two states as radiation (photon). This fast electronic transition is then followed by the slower rearrangement of the atomic configuration from D to O along  $E_g$ , with the excess energy dissipated as heat [Bla94, Has90]. However, if the temperature of the system becomes too high, a nonradiative transition can occur. The increased temperature can cause the thermal vibrations of the surrounding atoms to stimulate the excited luminescent center from A to C (Figure 2-5), along the curve  $E_e$ . At the crossing point C of curves  $E_e$  and  $E_g$ , the luminescent center may transit from a vibrational state of the excited state to a different vibrational state of

the ground state, subsequently being relaxed along  $E_g$  to the stable state, O, with the vibrational energy dissipated into the host lattice as heat [Bla94, Has90].

### **Luminescent Transitions**

When an incident electron strikes an inorganic material and produces hundreds of free electrons and free holes, they can recombine to produce luminescence (give off photons). However, there are a number of possible transitions in which this recombination can take place. A schematic of the possible transitions is shown in Figure 2-6 and each transition described below [Bru92, Has90, Yac90]:

**Transition 1. *Intraband transition:*** An electron is excited way above the conduction band level, travels down to the conduction band edge and attains thermal equilibrium with the lattice. This process is called thermalization and can lead to phonon-assisted emission but usually results in phonon emission.

**Transition 2. *Inter band transition:*** Direct recombination occurs between an electron in the conduction band and a hole in the valence band, thus producing intrinsic luminescence.

**Transition 3. *Exciton Decay:*** Excitons form at low temperatures and are a bound state with an electron-hole pair. This state exists just below the conduction band. Free excitons as well as excitons bound to an impurity may undergo this decay process.

**Transition 4. *Lambe-Klick Model:*** Recombination occurs from a donor impurity to a free hole.

**Transition 5. *Schon-Klasens Model:*** Recombination occurs from a free electron to an acceptor impurity producing extrinsic luminescence.

**Transition 6. *Prener-Williams Model:*** Recombination occurs between donor and acceptor impurities (i.e. rare-earth or transition metal).

**Transition 7.** Excitation and de-excitation of an impurity with incomplete inner shells is represented.

### **Cathodoluminescent Degradation**

In order for FEDs to become a viable technology, one of the main issues that needs to be addressed is the short brightness lifetimes of the phosphors in FEDs. The scientific understanding of this phenomenon has improved in recent years, but a solution to the problem has yet to be achieved. Proposed mechanisms for the loss of brightness, or cathodoluminescent degradation on sulfide-based phosphors, have included electron stimulated surface chemical reactions, accumulation of graphitic carbon, and charging effects.

One of the main problems preventing FEDs from becoming the dominant flat panel display technology is the short brightness lifetimes of the phosphors in FEDs. The typical FED uses beam energies that are much lower than the cathode ray tubes (~ 5 keV for FEDs and ~ 25 keV for CRTs) as well as a higher beam current. These differences, in addition to poor vacuum conditions in the FED, contribute to the increased rate of cathodoluminescent brightness loss. When operating at lower electron beam energies, the interaction volume of the electrons is reduced and subsequently the formation of a nonluminescent layer has greater effect on the brightness lifetime. Also, when operating at higher electron currents, it leads to saturation effects and enhanced phosphor degradation [Hol99]. The difficulties in maintaining a good vacuum level in the FEDs, due to difficulty in pumping out the device, also helps to contribute to the rapid decay of the CL brightness. In the scientific literature, several CL degradation mechanisms, such as electron stimulated surface chemical reactions, accumulation of graphitic carbon, charging effects, and point defects, have been proposed.

### Electron Beam Stimulated Surface Chemical Reactions

The most widely reported and accepted CL degradation mechanism in the scientific literature is known as electron beam stimulated surface chemical reactions [Seb95, Hol99, Hol00, Swa00]. During electron beam bombardment, adsorbed molecular species on the phosphor surface are dissociated into more reactive atomic species, which then react with the phosphor to form a non-luminescent layer, or “dead layer.”

Okada et al. were the first to report the formation of a nonluminescent layer on ZnS due to electron beam induced reactions [Oka79]. In their research, it was shown that in the presence of water vapor, a reacted layer was observed on a ZnS (110) cleaved surface. Using AES, it was found that a 200 Å thick reacted layer was grown after 40 minutes exposure to a 3 keV electron beam at a current density of  $1.4 \cdot 10^{-2} \text{ A/cm}^2$  [Oka79].

The degradation of sulfide based phosphors was further studied by many researchers [Seb95, Swa96, Tro96, Hol96, Oos97, Swa99, Hol00]. Both research groups focused their work on the standard CRT phosphors: ZnS:Al,Au (P22G), ZnS:Ag,Cl (P22B), and Y<sub>2</sub>O<sub>2</sub>S:Eu (P22R) and found that the interaction of the electron beam with the molecular species adsorbed on the surface of the phosphors increased the rate of degradation. This process has since been coined electron beam surface stimulated chemical reactions (ESSCR) by Holloway et al. and Swart et al.

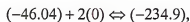
A detailed explanation of ESSCR was first described by Sebastian et al. Using phosphor films of ZnS on Si (100), they were subjected to electron bombardment at 2 keV over a range of pressures from  $1 \cdot 10^{-6}$  to  $1 \cdot 10^{-9}$  Torr. During the degradation experiments, hydrogen and oxygen were introduced into the vacuum to determine the

effects each gas has on surface modifications. The effects of the introduced gases were monitored using Auger electron spectroscopy (AES). By monitoring the ratio of the sulfur to the zinc Auger peaks, it was seen that the ratio decreased over the degradation time. This indicated that ZnS surface was becoming depleted of sulfur. However, it was found that the water vapor was the most active species (among hydrogen and oxygen). From these results, it suggests that the electron beam dissociated the adsorbed species on the ZnS surface into more reactive atomic species, which reacted with the sulfur in the ZnS thin film [Seb95].

Swart et al. performed similar experiments to Sebastian et al., but instead of using thin films, phosphor powders were used. In this study, ZnS:Cu,Al,Au and ZnS:Ag,Cl were degraded at a residual gas pressure of  $1.2 \cdot 10^{-8}$  Torr and oxygen pressures of  $10^{-6}$ . AES and CL measurements were made during the degradation of the phosphors to monitor changes in the surface state and the luminous efficiency. The AES results showed that there was an initial decrease in carbon on the phosphor surface followed by a decrease in sulfur with a simultaneous increase in oxygen and zinc. The AES results are shown in Figure 2-7. The postulated mechanism for this change in the surface composition is electron beam dissociation of molecular species to atomic species, i.e.,



which subsequently react with C to form volatile compounds ( $CO_x$ ,  $CH_4$ , etc.) or with ZnS to form either ZnO or  $ZnSO_4$ . The following are possible reactions, along with the free energies of formation for reactants and products for ZnS [Swa96]:



$$\Delta H = -94.43 \text{ kcal / mol O}_2,$$



$$2(-46.04) + 3(0) \rightleftharpoons 2(-83.24) + 2(-70.94),$$

$$\Delta H = -72.09 \text{ kcal / mol O}_2.$$

Trottier et al. studied the degradation characteristics of the three standard CRT phosphors. In their research, it was found that the degradation of the ZnS based phosphors was three times faster than  $\text{Y}_2\text{O}_2\text{S:Eu}$ . Again in this research, AES and CL data were collected simultaneously during the degradation experiments. The phosphors were exposed to electron bombardment (2 keV, 2 mA/cm<sup>2</sup>) at residual background gas pressures from  $2 \cdot 10^{-8}$  to  $10 \cdot 10^{-8}$  Torr. Even though the  $\text{Y}_2\text{O}_2\text{S:Eu}$  had a slower degradation rate than the two ZnS based phosphors, they all formed a non-luminescent layer on the surface. It was suggested that the oxysulfide was less affected by this surface change. Two possible reasons are that (1) the  $\text{Y}_2\text{O}_3$  formed on the oxysulfide surface was less optically absorbing than the ZnO formed on ZnS, or (2) the inherent differences in the emission mechanisms make  $\text{Y}_2\text{O}_2\text{S:Eu}$  less susceptible to changes in the lattice around the luminescing centers. The ZnS based phosphor's emission is characterized as a donor-acceptor pair emission where intentional defects are induced to produce localized energy levels in the band gap, which can luminesce. However, the  $\text{Y}_2\text{O}_2\text{S:Eu}$  luminesces by virtue of an atomic transition of the Eu atom. The transition is well-localized with the electrons confined to the same small center before and after the transition [Tro96].

The ESSCR model was further developed by Oosthuizen et al. [Oos97]. In their research,  $\text{ZnS:Cu,Al,Au}$  was subjected to a 2 keV electron beam at an oxygen pressure of

$1 \cdot 10^{-6}$  Torr. In addition to monitoring the APPH, the sample was analyzed using X-ray photoelectron spectroscopy (XPS) before and after degradation. The XPS data showed that the Zn peak in ZnS had shifted after the degradation to a higher eV corresponding to the Zn peak of ZnO. This, along with the AES data, indicated that the surface of the phosphor formed a non-luminescent layer of ZnO. The XPS also showed that the sulfur peak for ZnS decreased during degradation and there was no extra sulfur peak formed at 169.5 eV for ZnSO<sub>4</sub> [Oos97]. In addition, Oosthuizen et al. used residual gas analysis (RGA) to monitor any changes in gas molecules during the degradation experiment. The RGA results showed that SO<sub>2</sub> was formed during degradation. The increase in SO<sub>2</sub> supports the second proposed chemical reaction (Equation 2.15) by Trottier et al.

A mathematical model of the ESSCR was developed by Holloway et al. showing the dependence of degradation on gas type, gas pressure, current density and electron beam energy [Hol00]. Using AES combined with CL spectroscopy, Holloway et al. measured the correlation between the changes in the surface chemistry of the phosphors and the decrease in CL intensity. In order to develop a mathematical model of ESSCR based on these AES and CL results, it was assumed that since the bulk properties of the phosphor are not involved, that a surface science approach could be taken. Therefore, a standard chemical reaction rate expression could be used to express the concentration of sulfur species on the phosphor surface:

$$\frac{dC_s}{dt} = -kC_sC_{as}^n, \quad (2-16)$$

where  $k$  is a chemical rate constant,  $C_{as}^n$  is the concentration of the adsorbed atomic species that will react with ZnS,  $n$  is the order of the surface reaction, and first order

surface reactions are assumed. Assuming that the reaction takes place on the surface (versus in the gas phase),  $C_{as}$  can be written as:

$$C_{as} = Z\phi_{ma}C_mJ\tau_{as}, \quad (2-17)$$

where  $Z$  is the number of reactive atomic species produced from the parent molecule,  $\phi_{ma}$  is the dissociation cross-section of the molecule to atoms (which is a function of electron energy,  $E_p$ ),  $C_m$  is the surface concentration of the molecular species,  $J$  is the current density causing the dissociation, and  $\tau_{as}$  is the lifetime of a reactive atomic species, which is assumed to be very short. In other words, it can be assumed that the reaction rate is limited by the rate of production of adsorbed atomic species. The adsorbed molecule concentration,  $C_{as}$  and can be written as [Hud92]:

$$C_m = \sigma \left( \tau_o \exp \left[ \frac{Q}{kT} \right] \right) \left( \frac{P_m}{[2\Gamma mkT]^{1/2}} \right), \quad (2-18)$$

where  $\sigma$  is the molecular sticking coefficient and the first term in brackets is the molecular mean stay time on the surface, while the second term in brackets is the molecular flux onto the surface. Specifically,  $\tau_o$  is the mean time between attempts by the physisorbed molecule to escape from the surface,  $Q$  is the energy required to desorb from the surface,  $k$  is Boltzmann's constant,  $T$  is absolute temperature, and  $P_m$  is the partial pressure of the molecular gas in the vacuum. Equation 2-18 is Henry's isotherm, and assumes that the sticking coefficient is independent of coverage. Furthermore, it is assumed that the coverage of molecular species is well below a monolayer. Substituting equations 2-17 and 2-18 into 2-16 leads to [Hol00]:

$$\frac{dC_s}{dt} = -k\sigma C_s Z\phi_{ma}J\tau_{as} \left( \tau_o \exp \left[ \frac{Q}{kT} \right] \right) \left( \frac{P_m}{[2\Gamma mkT]^{1/2}} \right). \quad (2-19)$$



Equation 2-19 may be written as:

$$\frac{dC_s}{C_s} = -kK' JP_m dt, \quad (2-20)$$

where  $K'$  is defined by:

$$K' = k\sigma C_s Z\phi_{ma} J\tau_{as} \left( \tau_o \exp\left[\frac{Q}{kT}\right] \right) \left( \frac{P_m}{[2\pi mkT]^{1/2}} \right). \quad (2-21)$$

Integrating equation 2-20 with respect to time yields:

$$C_s = C_s^0 \exp[-K' P_m Jt], \quad (2-22)$$

where the boundary condition of  $C_s = C_s^0$  at time equal to zero was applied. Note that  $Jt$  is current density times time and is equal to coulombs per unit area, i.e., is equal to the electron dose, often called the coulombic dose. This model predicts that the concentration of sulfur will decrease exponentially with coulombic dose, and the rate of loss will be larger at higher gas pressures [Hol00]. These predictions are verified experimentally for ZnS in Figures 2-8 and 2-9. From Figures 2-8 and 2-9, one can see that the electron dose required for a given amount of degradation decreased as the pressure increased, which corresponds to the predicted mathematical model. The correlation between the Auger signal decline and the decreased CL intensity is shown in Figure 2-10. Since the CL intensity and the sulfur Auger peak intensity increased over the same reaction range, it can be assumed that these two decreases are interrelated.

Therefore, one can substitute  $I_{CL}$  for  $C_s$  in Equation 2-22 and write:

$$I_{CL} = I_{CL}^0 \exp[-K'' P_m Jt], \quad (2-23)$$

as was observed in Figure 2-8 [Hol00].

Figure 2-11 shows the linear dependence predicted in Equation 2-23 of the extent of reaction upon the gas pressure for a constant degree of reaction (i.e., a 50% decrease in the sulfur APPH). Finally, the rate of decrease of CL intensity for primary electron energies of 1, 2, or 4 keV in  $1 \cdot 10^{-6}$  Torr  $O_2$  is shown in Figure 2-12. This figure shows that ZnS degraded much faster at 1 keV case as compared to 4 keV [Hol00].

### **Carbon Accumulation**

Another degradation mechanism based on surface reactions was proposed by Seager et al. [Sea 97]. In these experiments,  $ZnS:Ag$ ,  $SrGa_2S_4:Eu$ ,  $ZnO:Zn$  and  $Y_2O_3:Eu$  were bombarded by an electron beam while measuring the optical absorbance. The results showed that the optical absorption of the area being degraded increased with time. This could often be observed as a visible darkened spot on the surface of the phosphor screens. Raman spectroscopic data suggests graphitic carbon was present in these darkened areas, which would cause absorption of ambient light (resulting in a dark spot) and absorption of light emitted by the phosphor (i.e., reduced CL intensity). It is believed this graphitic layer forms from the electron beam stimulated conversion of hydrocarbons adsorbed from the ambient.

These results of carbon accumulation on the surface contradict the results from Trottier et al. [Tro96] and Swart et al. [Swa96] where Auger electron data showed that the use of the electron beam on loose powders removed all traces of carbon. Therefore, to confirm the formation of the graphitic carbon layer, Seager et al. conducted degradation experiments of  $YSiO_5:Tb$  and  $Y_2O_3:Eu$  screened powder under similar conditions at five collaborating institutions. The data confirmed that the CL intensity decreased rapidly with increasing electron bombardment, and a dark spot was observed on the surface of the screen. Post-degradation analysis of the amount of carbon present

inside versus outside the degraded area showed that either no change or more generally an increase in carbon. It was concluded that degradation of screened phosphors caused a buildup of near-surface carbon, which may absorb/scatter photons emitted by the phosphor. The carbon resulted from trace amounts of the hydrocarbons used to prepare the screened powders. The loss of CL intensity from the carbon in this case shows that having a pristine surface is vital in preventing electron beam stimulated surface chemical reactions [Hol99, Sea01].

### **Point Defects**

This degradation mechanism has been proposed that it takes place in conjunction with the previously discussed electron beam stimulated surface chemical reactions. According to ESSCR, during coulombic aging, the CL brightness decreases over time due to the formation of a non-luminescent layer on the phosphor surface. However, the magnitude of this CL loss cannot be explained solely due to the non-luminescent layer formation. Swart et al. showed that the ZnO was not sufficiently thick to explain the magnitude of the decline of the CL intensity [Swa96]. Therefore, a defect theory has been proposed to reconcile the difference [Swa96, Wan97, Hol99, Swa99, Hol00, Swa00].

Swart et al. proposed that the dead layer be complemented by point defects which were injected into the near-surface region in proportion to the amount of ZnO formed on ZnS [Swa96]. Sebastian used secondary ion mass spectrometry (SIMS) and thermoluminescent data from ZnS thin films before and after degradation to conclude that the ESSCR caused incorporation of oxygen into the near-surface region [Seb97, Hol00]. This subsurface oxygen formed isoelectronic traps, which reduced the excitation efficiency for the dopant in ZnS and thereby caused a reduced CL intensity. The

thermoluminescent data for as processed and degraded ZnS:Mn are shown in Figure 2-13. The peak observed at about  $-85^{\circ}\text{C}$  for as-processed ZnS is attributed to vacancies on the sulfur sub-lattice. After degradation, the  $-85^{\circ}\text{C}$  peak is replaced by two peaks, one at  $-110^{\circ}\text{C}$  and another at  $-60^{\circ}\text{C}$ , which are attributed to oxygen substituted on the sulfur sub-lattice [Seb97, Hol00]. Since the data fits the predictions of the model, it is assumed that the extent of the incorporation of oxygen in isoelectronic traps is directly proportional to the extent of formation of ZnO in the surface layer [Seb97]. This prediction seems possible since oxygen isoelectronic traps must be incorporated during ZnS lattice dissociation, and the amount of ZnO formed should be proportional to the amount of lattice disruption [Hol00].

### Charging

The CL degradation of the sulfide-based phosphors is not limited to electron stimulated surface reactions, but it can also be caused in part to surface charging [Swa99, Swa00, Hol99]. During the CL degradation experiment of ZnS:Ag, the electron beam was turned off for an extended period of time and as soon as electron bombardment was resumed, the measured CL intensity was about 20% higher than before the beam was shut off, but decreased within seconds and stopped at the same intensity as before the beam was shut off. This charging effect can be seen in Figure 2-14. These results show that the decrease in CL intensity is partially the result of surface charging. The charge accumulation on the surface alters the surface potential, which in turn does not only alter the kinetic energy of the primary electrons but also has an effect on the electron-hole pair created during the CL process. Figure 2-15 shows the energy band diagram of a semiconductor whose surface is negatively charged. The negative charge repels the free electrons near the surface and leaves positively charged donor ions behind. The region

near the surface therefore has fewer electrons (depletion layer) than the interior of the solid causing band bending to occur as shown in Figure 2-15. In the CL process, the electrons that are excited to the conduction band in the depletion layer will experience a repulsive force near the surface and the probability that the electron-hole pairs will be swept apart before recombination increases with the consequent loss in CL intensity. The surface charging will also directly alter the CL efficiency if the surface potential becomes large enough to alter the arrival energy of the exciting electrons [Swa99].

### **Transparent Conducting Oxides**

#### **Background/History**

Transparent conducting oxide (TCO) films that are both transparent in the visible region and electrically conducting have been widely studied for over 20 years as a result of their extensive applications in optoelectronic devices. These include energy-efficient windows, burglar alarms, window heaters, electrodes for solar cells and especially for flat panel displays such as liquid crystal displays, plasma display panels, field emission displays, organic electroluminescent devices, etc [Che00]. As the market for TCOs has grown, so has the interest in developing possible new TCOs (e.g.  $\text{CuAlO}_2$ ,  $\text{Cu}_2\text{SrO}_2$ ,  $\text{Cd}_2\text{SnO}_4$ ,  $\text{CdO}$ ,  $\text{ZnSnO}_4$ ,  $\text{GaInO}_3$ , etc.) with higher electrical conductivities and higher optical transmission in the visible region. However, this research will focus on using indium tin oxide (ITO), the most widely used TCO in optoelectronic devices [Lew00] and aluminum doped zinc oxide (ZAO), which has the potential to replace ITO in FPD and solar cell applications [Gor00] as coating materials.

An ITO thin film is a highly degenerated n-type semiconductor, which has a low electrical resistivity of  $\approx 10^{-4} \Omega\text{-cm}$  and a high optical transmittance of  $\approx 85\%$  in the visible region [Kim00a]. The electron carrier concentration of highly conductive ITO films

ranges from  $\approx 10^{20}$  to  $\approx 10^{21} \text{ cm}^{-3}$ . Moreover, ITO is a wide band gap semiconductor ( $E_g=3.5\text{--}4.3 \text{ eV}$ ) showing high optical transmittance in the visible and near-IR regions of the spectrum [Kim00a].

Recently, ZAO films have attracted interest as a TCO because the material consists of a cheap and abundant element that is readily produced for large-scale coatings, has a low growth temperature, and has high stability in hydrogen plasma [Jeo01]. ZAO films are also wide band gap semiconductors with a band gap of 3.4 eV [Loo01]. Their typical electrical resistivity is in the range of  $2\text{--}5 \cdot 10^{-4} \Omega\cdot\text{cm}$  [Hir97, Kim00a, Kim00b] and their optical transmittance is in the range of  $\approx 85\%$  in the visible region [Mal00].

To obtain the unique combination of high electrical conductivity and optical transmittance seen in ITO, ZAO, and other TCOs, it is necessary to have an oxide material with a wide-band gap ( $>3\text{eV}$ ) that can be rendered degenerate (that is, the states at the bottom of the conduction band are filled) through the introduction of native or substitutional dopants. The materials should also have a conduction band shape (dictating electron effective mass) that ensures that the plasma-absorption edge lies in the infrared range [Lew00]. This yields a transmittance in the visible often greater than 90%. The low electrical resistivity ( $\rho \sim 10^{-3}\text{--}10^{-4} \Omega\cdot\text{cm}$ ) of these materials is derived from extremely high carrier concentrations ( $N \sim 10^{20}\text{--}10^{21} \text{ cm}^{-3}$ ), since the carrier mobilities are low ( $\mu \sim 5\text{--}50 \text{ cm}^2/\text{V}\cdot\text{s}$ ). Until very recently, useful conductivities could only be achieved for *n*-type materials. This has changed with the development of *p*-type TCO materials over the past few years [Kaw00].

The first mention of a conducting oxide was reported by Badeker in 1907, when Badeker reported that thin films of Cd metal grown in a glow discharge chamber could be

oxidized to become transparent while remaining electrically conducting [Bad07, Lew00]. Since then, the commercial value of TCO thin films has been recognized, which has led to the development of new TCO materials. Today, the most widely used TCO in optoelectronic devices is ITO [Lew00]. ITO was first developed in 1951 by Mochel, and still maintains some of the best performance characteristics for optical and electrical conductivity [Moc51, Gor00]. Due to its excellent optical and electrical properties, ITO is being used in the majority of applications needing a TCO.

Transparent conducting oxide thin films are used in a variety of applications. The largest application is for heat reflecting, low emissivity coatings for architectural glass. For this application, large areas of glass will be coated and therefore, a low cost and easily deposited TCO needs to be used. In this case, the TCO does not require good electrical properties, but only a high carrier concentration in order to achieve low emissivity in the infrared region. [Lew00, Gor00]. To satisfy these criteria, fluorine doped tin oxide, silver, and titanium nitride have been used [Lew00, Gor00, Cho83]. Another large application for TCOs is in the flat panel display industry. Even though there are many different types of FPDs, they all use TCOs as the front electrode. In addition to high electrical conductivity and optical transparency, this application requires the TCO to have a low deposition temperature, to prevent the adverse affects on the thermally sensitive organic dyes, and ease of etching. The material most often used for these reasons is ITO [Gor00].

### **Optical Properties**

In order for a material to have high optical transmittance in the visible region, the material must have a wide band gap ( $E_g \geq 3$  eV), a plasma frequency in the infrared

region, and minimal defects in the thin films. How each of these factors effects the optical transmittance will be discussed below.

For a photon to be transmitted through a material, it must possess an energy that is less than the band gap energy of the material (and above the plasma frequency – explained below). The photon energy range for visible light is 1.77 eV to 3.1 eV. Hence, for visible light to pass through a material, the band gap of the material must be  $\sim 3$  eV or greater.

However, the band gap of the TCOs can shift (widen) due to the introduction of intrinsic or extrinsic dopants. This shift is called the Burstein-Moss effect. As the carrier concentration (dopants) increases, the Fermi energy moves above the conduction band edge, resulting in the complete occupation of states at the bottom of the conduction band. Therefore, optically stimulated transitions to these states cannot occur, and the optical band gap of the material increases [Cho83, Lew00, Gra02]. This process is shown schematically in Figure 2-16. The vertical area shows the allowed transition from the valence band to an energy in the conduction band above the Fermi energy. The amount of the shift is a function of the doping concentration, and the density-of-states effective mass ( $m_{cv}^*$ ) as shown in Equation 2-24 [Jar76, Cho83, Hum93].

$$\Delta E_g = \frac{h^2}{8 \cdot m_{cv}^*} \cdot \left( \frac{3 \cdot n}{\pi} \right)^{\frac{2}{3}} \quad (2-24)$$

The density-of-states effective mass reflects the fact that effective mass of a conduction band electron can be a function of conduction band density-of-states in some situations [Ell93].



For a material to be a useful TCO, in addition to having a wide band gap, it must also have its plasma frequency in the near-infra-red region. The plasma frequency is the characteristic frequency in a material, which separates the reflective and transparent region. In other words, it is the minimum frequency a photon must have in order for it to transmit through the thin film. Figure 2-17 shows a schematic representation of the transition from the reflective case to the transparent case according to the free electron theory without damping [Hum93].

The optical phenomena in TCOs in the near infrared region of interest are based on the classical Drude theory of free electrons [Cho83] and Maxwell's equations [Cou00]. The use of the Drude theory is validated by the fact that TCOs are similar to metals in that they possess nearly free electrons. Then by using Maxwell's equations, the complex permittivity can be defined as a function of frequency and conductivity [Cou00]. The motion of the free electrons can then be modeled using the Lorentz oscillator model, which leads to an expression for the complex conductivity that is a function of carrier concentration, relaxation time, effective mass of free carriers, and frequency of the electric field [Hum93, Cou00]. From the complex conductivity, expressions can be derived for the real and imaginary parts of the refractive index, which in turn leads to the real and imaginary parts of the permittivity, respectively [Cou00]:

$$\epsilon_1 = \epsilon_\infty \left( 1 - \frac{\omega_p^2}{\omega^2} \right) \quad 2-25$$

and

$$\epsilon_2 = \left( \frac{\epsilon_\infty \omega_p^2}{\omega^2 \tau} \right) \quad 2-26$$

These equations assume that the electrons are completely free and that  $\frac{1}{\tau} \ll \omega$ , where  $\tau$  is the relaxation time and  $\omega$  is the frequency of the electric field.  $\omega_p$  is the plasma frequency and is given by

$$\omega_p = \left( \frac{ne^2}{\epsilon_0 \epsilon_\infty m_c^*} \right)^{\frac{1}{2}} \quad 2-27$$

where  $n$  is the carrier concentration,  $e$  is the electronic charge,  $\epsilon_0$  is the permittivity of free space,  $\epsilon_\infty$  is the high-frequency permittivity, and  $m_c^*$  is the conductivity effective mass [Cou00].

Equation 2-26 shows that  $\epsilon_1$  is large and negative for  $\omega < \omega_p$ , but approaches  $\epsilon_\infty$  when  $\omega > \omega_p$ . However,  $\epsilon_2$  is large and positive for  $\omega < \omega_p$ , but tends to zero for  $\omega > \omega_p$ . The real and imaginary parts of the refractive index can be derived from equations 2-26 and 2-27 [Cou00]. The derivations are

$$N = \sqrt{\frac{1}{2}(\epsilon_1^2 + \epsilon_2^2)^{1/2} - \frac{\epsilon_1}{2}}, \quad 2-28$$

which is the refractive index, and

$$k' = \sqrt{\frac{1}{2}(\epsilon_1^2 + \epsilon_2^2)^{1/2} - \frac{\epsilon_1}{2}}, \quad 2-29$$

which is the extinction coefficient. From equations 2-26 through 2-29, one can see that, at high frequencies, the TCOs behave like a perfect dielectric, whereas at sufficiently low frequencies, where both  $N$  and  $k'$  are large, the material has near-unity reflectance [Cou00].

If the electrical properties of the TCO thin film are known, then one can use these equations to model their optical properties. Figure 2-18a shows a plot of film reflectance versus wavelength, where the wavelength at which the transition occurs changes with carrier concentration. Notice that as the carrier concentration increases, the transition associated with the plasma frequency shifts to shorter wavelengths [Cou00]. In Figure 2-18b (Cou00fig3), absorptance is plotted versus wavelength, and shows the effects of carrier concentration on free-carrier absorption. As the carrier concentration was increased, the height of the free-carrier absorption band increased because there were more carriers to absorb the photons, as well as, a decrease in peak width [Cou00]. These figures show that in the visible wavelengths, the films are largely free of absorption. This is because the electrons are unable to stay in phase with the electric field at these high frequencies and, consequently, are unable to absorb energy [Cou00]. Figure 2-18c also plots absorptance versus wavelength, and shows changes in absorptance with mobility. This figure shows that as the mobility is increased, the height of the free-carrier absorption band decreased. Therefore, to increase the conductivity of a TCO without effecting the optical properties, it is better to attempt to increase the carrier mobility rather than the carrier concentration. By looking at the equation for mobility:

$$\mu = \frac{e \cdot \tau}{m_c^*} \quad (2-30)$$

where  $e$  is the electronic charge,  $\tau$  is the relaxation time (time between collisions of electrons with a scattering center), and  $m_c^*$  is the effective mass. This equation shows that in order to increase the carrier mobility, either the relaxation time must be increased or the effective mass must be decreased. So when finding a new material with a lower effective mass is not an option, one must decrease the relaxation time [Cou00]. This can

be achieved by improving the quality of the films (i.e. fewer defects, improved orientation, etc.).

Minimizing the amount of defects is important in obtaining an optically transparent film. Defect absorption for TCOs can take two forms, absorption of light that promotes an electron to a defect level, and absorption by metallic particles in the TCO. In the first case, when impurities or defects (in the lattice) are present in the TCO, then a photon with the proper energy can promote an electron from the valence band (or another defect state) into a defect state, with the photon being absorbed. In second case, since TCOs are intentionally made to be substoichiometric with respect to oxygen, that when the material is far enough off in stoichiometry, highly reflective scattering precipitates can form [EII93].

### **Electrical Properties**

In order to achieve the lowest resistivity in TCOs, the goals are the minimization of microstructural features and impurities that lead to reduced electron mobility, the maximization of activated substitutional metal dopants, and the creation of optimal oxygen substoichiometry [Gor00, Lew00].

The electron mobility is determined by the electron-scattering mechanisms that operate in the material. Even in pure single crystals, there are some scattering mechanisms, such as scattering of electrons by phonons [Gor00]. This is caused by the light-induced vibrations of the lattice atoms, i.e., by the excitation of phonons by photons. When a photon of the appropriate wavelength causes the atoms to perform oscillations about their points of rest, this perturbation causes the photons to undergo a dampening effect and thus reduces the mobility of the electrons [Hum93]. In addition to phonon scattering, the maximum mobility can be lowered further by other scattering mechanisms

such as grain-boundary scattering, which is present in polycrystalline thin films. The smaller the grain sizes, the higher the probability that the electron will encounter a scattering event resulting in a decrease in mobility [Mah99].

TCOs, when prepared intrinsically, i.e. without intrinsic or extrinsic dopants, have very high resistivities (of the order of  $> 10^7 \Omega\text{cm}$ ). The low resistivity, which is required for their application as transparent electrodes, can be achieved in two ways. First, by creating intrinsic dopants through lattice defects (for instance oxygen vacancies or metal atoms on substitutional lattice sites). Second, by the introduction of extrinsic dopants (either metals with one additional conduction electron on the metal lattice sites or halogens with one additional electron on oxygen lattice sites) [El100].

The first case can be achieved during the deposition by carefully controlling the oxygen partial pressure and the deposition rate [El100]. Similar results have also been achieved through a reduction process of the oxide after deposition. This can be done by annealing the oxide thin film under vacuum or in a hydrogen-containing atmosphere. However, the lowest electrical resistivity using this method is only about  $10^{-2}$ - $10^{-3} \Omega\text{cm}$ . In addition, these films are not stable under ambient conditions due to the re-oxidation of the oxygen-deficient films [Cap82]. Therefore, in most cases extrinsic dopants are used for the preparation of TCOs. These extrinsic dopants are typically already present in the optimum concentration in the target material and are therefore properly incorporated into the metal oxide thin film during physical vapor deposition processes. However, during the deposition of the TCO, the oxygen partial pressure can be varied controlling the amount of oxygen incorporated into the film. As the oxygen partial pressure increases, the charge carrier concentration decreases, which is attributed to an oxidation of the metal

dopants. Thus, the metal oxide no longer behaves as a dopant. Then when the oxygen partial pressure is lowered below its optimum level, the TCO becomes more and more opaque due to the increasingly oxygen deficient films [Eli93, Gor00, Lew00, Eli00, Cha01]. For example, in the case of ZnO:Al, at low oxygen partial pressures, there is a preferential build-in of Al into the layers because of the higher affinity oxygen has for Al than Zn. Therefore, the reduction in available oxygen leads to a decrease in the ZnO phase and a corresponding increase of the unoxidized, i.e. metallic, zinc. It is this metallic zinc that leads to the darkening of the films at low oxygen partial pressures [Eli00].

As can be seen from the overview of TCOs, their use as coating materials of sulfide-based phosphors can serve many purposes. Not only will the coating layer serve as a barrier to prevent surface reactions, but the optical transmittance in the visible spectrum is ideal for allowing the generated photons (light) from the phosphors to be emitted without much impedance and finally, the charging effects currently experienced by sulfide-based phosphors can be drastically reduced.

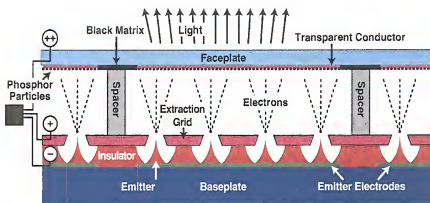


Figure 2-1. Schematic of a typical field emission display [Can02].

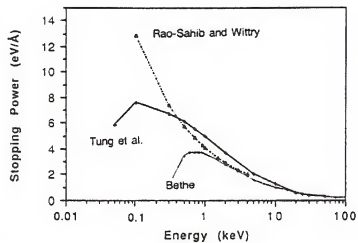


Figure 2-2. Comparison between different models for stopping power. [Joy89]



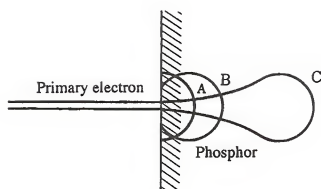


Figure 2-3. A schematic illustration showing the increase in interaction volume with the increase in electron beam energy [Has90].

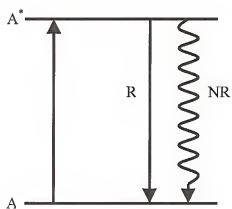


Figure 2-4. Schematic energy level scheme of the luminescent ion A. R – radiative return; NR – nonradiative return to the ground state.

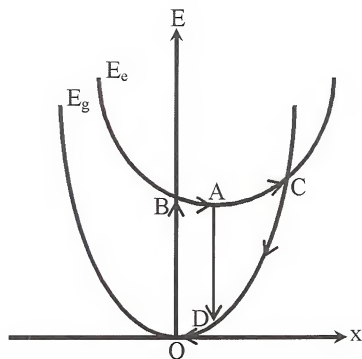


Figure 2-5. Configurational coordinate model of a luminescent center.

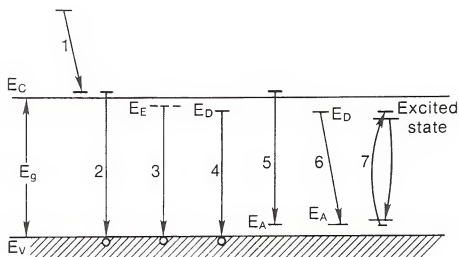


Figure 2-6. Schematic diagram of luminescence transitions between the conduction band ( $E_C$ ), the valence band ( $E_V$ ), and exciton ( $E_E$ ), donor ( $E_D$ ), and acceptor ( $E_A$ ) levels in the luminescent material [Bru92].

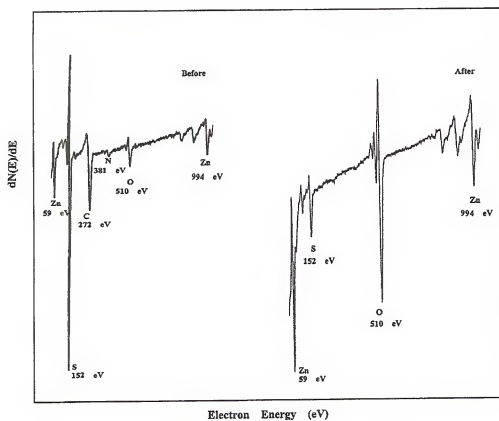


Figure 2-7. Auger spectra before and after electron beam aging of the ZnS phosphor [Swa96].

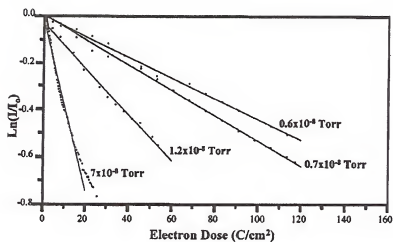


Figure 2-8. Semilogarithmic plot of normalized CL intensity vs. dose for P22B ZnS:Ag phosphor irradiated with 2 keV electrons in residual vacuum at pressures between  $6 \cdot 10^{-9}$  and  $7 \cdot 10^{-8}$  Torr [Hol00].

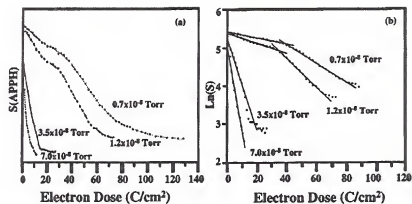


Figure 2-9a,b. Sulfur Auger electron peak height vs. dose of 2 keV electrons from P22B ZnS:Ag phosphor at residual vacuum pressures between  $7 \cdot 10^{-9}$  and  $7 \cdot 10^{-8}$  Torr. (a) Linear plot; (b) semilogarithmic plot [Hol00].

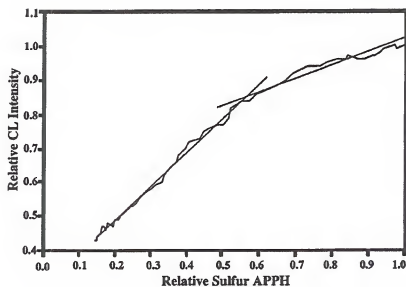


Figure 2-10. CL intensity vs. sulfur Auger electron beam peak height for ZnS:Mn thin films in  $1 \cdot 10^{-6}$  Torr  $O_2$  irradiated by 4 keV electrons. Note the linear relationship, however, extrapolation of the plot towards zero will result in an intercept at zero on the Auger peak height axis before the zero is reached on the CL intensity axis [Hol00].

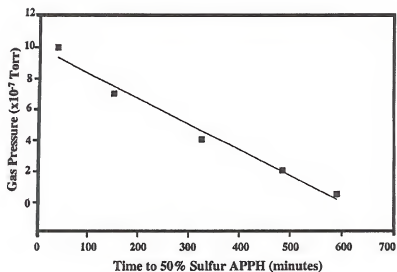


Figure 2-11. Plot of  $O_2$  pressure vs. the time to result in a 50% decrease of the sulfur Auger peak height for  $ZnS:Mn$  irradiated with 2 keV electrons. Note the linear dependence upon pressure [Hol00].



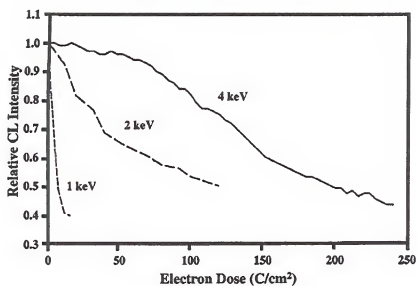


Figure 2-12. CL intensity vs. electron dose from ZnS:Mn in  $1 \cdot 10^{-6}$  Torr  $O_2$  for 1, 2, 4 keV primary beam electrons [Hol00].

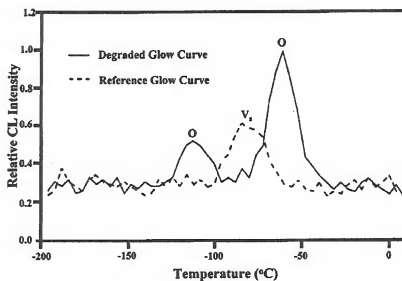


Figure 2-13. Thermoluminescent intensity vs. temperature (glow curves) of ZnS:Mn sample before and after degradation to  $\sim 160 \text{ C/cm}^2$  in  $1 \cdot 10^{-6}$  Torr  $\text{O}_2$  with 4 keV electrons [Hol00].

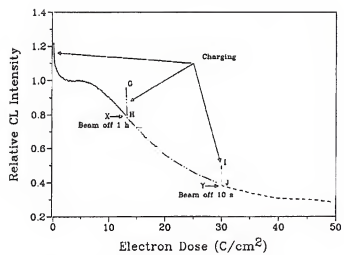


Figure 2-14. Charging effect on the CL intensity [Swa96].

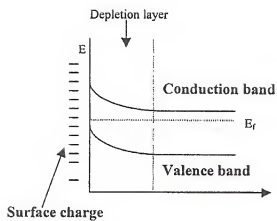


Figure 2-15. The electron band diagram of a semiconductor which surface is negatively charged [Swa99].

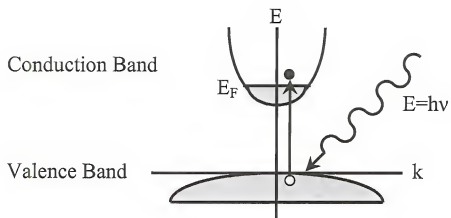


Figure 2-16. Illustration of the Burstein-Moss shift, which increases the optical band gap due to occupancy of states in the conduction band.

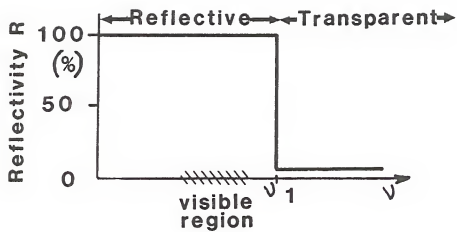
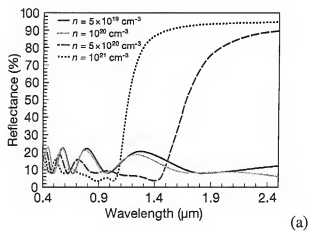
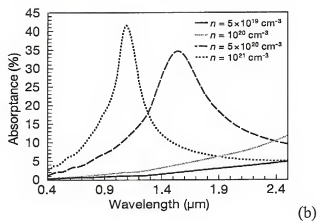


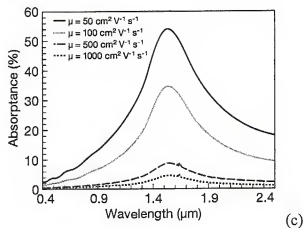
Figure 2-17. Schematic frequency dependence of an alkali metal according to the free electron theory without damping.  $\nu_1$  is the plasma frequency [Hum93].



(a)



(b)



(c)

Figure 2-18a-c. Theoretical plots of relationships between electrical and optical properties for (a) reflectance versus carrier concentration, (b) absorbance versus carrier concentration, and (c) absorbance versus carrier mobility [Cou00].

## CHAPTER 3 EXPERIMENTAL PROCEDURES

### Introduction

Cathodoluminescent degradation of coated and uncoated ZnS:Ag phosphors was studied in this work. The as-received ZnS:Ag phosphor degradation behavior was compared to the degradation behavior of the same ZnS:Ag phosphors that were coated with nano-meter thick coatings of indium tin oxide (ITO) and zinc oxide doped with aluminum (ZAO). These phosphors were analyzed at varying electron beam energies, pressures, and current densities.

### Sample Preparation

#### ZnS:Ag

ZnS:Ag blue powder phosphor was obtained from Osram Sylvania. Osram Sylvania manufactures uncoated ZnS:Ag which was preferred to reduce the number of variables that could influence degradation behavior as compared to ZnS:Ag blue powder phosphors from Kasai and Nichia who coat their blue phosphors with silica particles for better handling.

#### Coating Process

A modified pulsed laser deposition technique was used to deposit nano-meter thick thin film coatings on ZnS:Ag. This technique is quite unique because of its ability to deposit uniform continuous coatings on particulate surfaces. Other coating techniques [Kom97, Jea00, Vil02] are unable to produce the continuous coating or the nano-meter



thickness scale aspect needed in this research. A schematic of this coating process is shown in Figure 3-1.

This coating technique uses a Lambda Physik model LPX-305i pulsed excimer laser as the energy source to create a plume of excited species during processing. The output of the excimer laser has an operating wavelength of 248nm when operated with a krypton-fluoride gas mixture. The time duration of the output laser pulse is 25 ns with a rectangular shape and Gaussian distribution. A computer-laser interface allows control of the incident beam energy as well as the laser repetition rate that can be varied from 1-50 Hz. To ensure the proper energy during deposition, the laser output energy was calibrated and recorded by a Gentec laser energy meter with a SUN series reading head model # ED 500 before each deposition. As shown in Figure 3-1, the pulsed laser beam irradiates the solid sputtering target through the ultraviolet transparent quartz window. The laser-generated plume is directed onto the particles (substrate material) which are fluidized using a mechanical agitation system. As mentioned above, apart from the mechanical agitation system, this coating technique closely resembles that of a typical pulsed laser deposition system. To coat the ZnS:Ag phosphors, they are placed into the bowl within the mechanical agitation system as shown in Figure 3-2. Once the phosphor powder is in the bowl, the mechanical vibration is generated by controlling the voltage on a high-speed motor with a designed off-axis weight attached. By controlling the speed of the off-axis weight, the magnitude of the vibrational displacement can be modified. Due to the vibrational displacements, isolation of the motor is required using a system of springs. The speed of the motor was controlled by an Instek 0-18 volt dc power supply model # PS-18300. Once the phosphor powder was in the bowl, the vacuum system was

pumped down to  $1 \cdot 10^{-5}$  Torr and backfilled to the desired pressure with the appropriate gas. A MKS Baratron pressure transducer model # 626A with a range from 1 Torr to  $1 \cdot 10^{-3}$  Torr and a power supply readout model #933 PDR-D were used to measure the pressure in the low vacuum regime. A MKS cold cathode pressure gauge model # 421 with a power supply readout model # 943 with a range from  $5.0 \cdot 10^{-3}$  Torr to  $1 \cdot 10^{-8}$  Torr were used to measure the pressure in the high vacuum regime. The desired pressure in the vacuum system during the depositions was controlled using a MKS model # 247C mass flow controller with a 4-channel readout.

### **Experimental Characterization Techniques**

Many different characterization techniques were used to determine the optical and electrical properties of the deposited thin films, the cathodoluminescent lifetime of the phosphors, surface changes of the phosphor, as well as the effects of the residual gases during the phosphor degradation experiments.

#### **Cathodoluminescent Degradation Measurements**

Cathodoluminescent (CL) degradation measurements were performed on ZnS:Ag powder. The CL measurements were made using two different CL systems. The early studies on the degradation behavior of coated and uncoated ZnS:Ag were performed in a UHV vacuum system. A schematic of this system is shown in Figure 3-3. The base pressure of the vacuum system is  $1 \cdot 10^{-8}$  Torr. It uses a Kimball Physik model # ECGS-7H electron gun with beam energies from 0.5 to 5 keV and currents from 31.4nA to 314nA. The spot size was 1.5 mm in diameter and therefore corresponds to a current density in the range of 1 to  $10 \mu\text{A}/\text{cm}^2$ . The sample current was determined by biasing the electrically isolated sample carousel with a 120-volt battery with an ammeter in series to ground. The intensity of the emitted photons was measured using an Ocean Optics

model # S2000 fiber optic spectrometer with a charge-coupled device detector attached to a personal computer. Before and after each degradation experiment, background gas measurements were performed using a residual gas analyzer (RGA) model # 5432.

The samples were prepared by cold pressing the phosphor powder into a 1/16 in deep and 1/8 in wide hole (divot) in a stainless steel holder. The stainless steel holder was then placed onto the carousel in the vacuum chamber via a load lock chamber. After the sample is inserted into the vacuum system, the desired vacuum level was obtained by throttling the poppet valve between the ion pump and the vacuum chamber. Then the electron gun was turned on and the entire system was allowed to equilibrate for 12 to 24 hours to ensure that the electron beam current and the pressure level had stabilized. Once everything had stabilized, the carousel was rotated so that the electron beam struck the phosphor sample and then the computer software was started which recorded the CL intensity measurements.

CL degradation experiments were also performed in a JEOL 6400 Scanning Electron Microscope (SEM). A schematic of this system is shown in Figure 3-4. CL measurements were made using the electron beam of the SEM to excite the phosphors and measuring the resulting photons using a Gatan CL detector model # PANACL6 201 which was connected to a personal computer. Before and after each experiment, SEM micrographs, CL micrographs, EDX spectra, RGA spectra, electron-beam current measurements, and pressure measurements were also taken.

The samples were prepared by depressing the phosphor powders into a 1 cm by 1 cm piece of indium foil (99.999% purity). The indium foil with the phosphor powder was then mounted onto a 0.5 in thick aluminum SEM mount using conductive copper tape

(Ted Pella). The SEM mount with the sample was then introduced into the SEM via a load lock chamber. As in the previously mentioned CL system, the electron-beam current and the vacuum levels were allowed to stabilize before beginning with the CL measurements.

### **Scanning Electron Microscopy**

The Scanning Electron Microscope (SEM) used in this research was a JEOL 6400 SEM. The SEM uses secondary electrons produced as a result of electron-beam solid interactions to produce a topographic image of the sample.

Figure 3-5 shows a cross-sectional view of a typical SEM electron column, deflection system, and electron detectors. The electron gun is typically comprised of a thin (~0.25 mm) tungsten filament. When enough heat is supplied to this filament so that electrons can overcome the work-function energy barrier of the material and escape from the material, thermionic emission occurs. These electrons are then accelerated towards the sample by applying a positive potential on the anode (3-30keV) [Gol92].

Once the electron beam strikes the sample, secondary and backscattered electrons are created. These electrons are separated according to their energies. Electrons that are emitted from the sample with energies below 50 eV are the secondary electrons while those with energies above 50 eV are the backscattered electrons. The secondary electrons are used to obtain SEM images. When the electron beam is rastered across the sample, the emitted secondary electrons are collected by a detector, and the output can be used to modulate the brightness of a cathode ray tube (CRT) whose *x*- and *y*-inputs are driven in synchronism with the *x*-*y* voltages rastering the electron beam across the sample. In this way an image is produced on the CRT; every point that the beam strikes on the sample is mapped directly onto a corresponding point on the screen [Bru92].

### **Energy-Dispersive X-Ray Spectroscopy**

Most applications of Energy-Dispersive X-Ray Spectroscopy (EDS) are in electron column instruments like the SEM, the electron probe microanalyzer (EPMA), and transmission electron microscopes (TEM). In this research, the EDS system (JEOL 1000 EDS ) was interfaced with a JEOL 6400 SEM and used to compare relative peak heights of sulfur and zinc before and after the degradation of ZnS:Ag.

EDS spectra are obtained by measuring the energy of x-rays emitted from a sample during electron beam bombardment. These x-rays are produced as a result of the ionization of an atom by high-energy primary electrons that strike the sample and remove an inner shell electron. To return the ionized atom to its ground state, an electron from a higher energy outer shell fills the vacant inner shell and, in the process, releases an amount of energy equal to the potential energy difference between the two shells. This excess energy, which is unique for every atomic transition, will be emitted by the atom either as an X-ray photon or will be self-absorbed and emitted as an Auger electron. Thus, in an atom with many shells, many emissions can result from a single primary ionization [Bru92].

### **Auger Electron Spectroscopy**

Auger electron spectroscopy (AES) is a technique used to identify the elemental composition, and in many cases, the chemical bonding of the atoms in the surface region of solid samples. In this research, AES was used to verify the presence of the nano-meter thick coatings of indium tin oxide (ITO) and aluminum doped zinc oxide (ZAO) on ZnS:Ag phosphor particles. For this work, a Perkin Elmer PHI 660 Scanning Auger Multiprobe system was utilized.

The basic principle behind AES involves the production of an atomic inner shell vacancy, usually by electron bombardment, and the following decay of the atom from this excited state through an electronic rearrangement and subsequent emission of an energetic electron instead of a x-ray. For example, as shown in Figure 3-6, if a Si surface is bombarded by a high energy primary electron beam, some of the Si atoms will lose electrons from their K shell (binding energy  $\sim 1.8$  keV) due to the impact from the primary electron beam. This K shell vacancy will normally be filled by the decay of an electron from one of the L subshells. In this example, assume that an electron in the  $L_{2,3}$  shell decays, which has a binding energy of 104 eV. This leaves an energy excess of 1.7 keV. This excess energy can be alleviated by either the emission of an x-ray or through the ejection of another  $L_{2,3}$  shell electron that overcomes its 0.1 keV binding energy and carries off the remaining 1.6 keV of energy. The removed electron is called a Si  $KL_{2,3}L_{2,3}$  Auger electron. Since there are two vacancies in the  $L_{2,3}$  shell, there can be further decay processes that lead to more Auger electrons [Bru92].

These Auger electrons are then analyzed in a device called a cylindrical mirror electron energy analyzer. This device can be adjusted to only accept secondary electron energies in a narrow range of kinetic energies. As the analyzer voltage is swept across the range of interest, the  $n(E)$  vs.  $E$  distribution is obtained directly as shown in Figure 3-7a. However, in order to improve the signal to noise ratio in the raw data, the data is typically shown in the  $dn(E)/dE$  vs.  $E$  form as shown in Figure 3-7b.  $n(E)$  is the number of secondary (Auger) electrons being detected and  $E$  is the Auger electron energy [Hud92].

### X-Ray Photoelectron Spectroscopy

X-Ray Photoelectron Spectroscopy (XPS) is a nondestructive surface technique. It was used in this research to analyze the coated and uncoated phosphor particle surfaces before and after they were exposed for a prolonged time under an electron beam to determine if any chemical changes had taken place at the surface. Specifically, a PHI 5100 XPS system was used with unmonochromatized Mg K $\alpha$  (1253.6 eV) x-ray radiation at a power of 300 W. The pressure during analysis was  $5 \pm 10^{-9}$  Torr. The photoelectron take off angle was set at 45° and the binding energies were referenced to the adventitious C1s peak at 284.6 eV.

XPS uses a high energy (short wavelength) X-ray beam to strike the sample surface. This can cause an atom to become ionized, producing an ejected free electron. The kinetic energy KE of the electron (the photoelectron) depends on the energy of the photon  $h\nu$  expressed by the Einstein photoelectric law:

$$KE = h\nu - BE, \quad (3.1)$$

where  $BE$  is the binding energy of the particular electron to the atom concerned. Since  $h\nu$  is known and the  $KE$  of the photoelectrons can be measured, the  $BE$  of the material of interest can be calculated. For example, if a sample containing carbon atoms is being bombarded with X-rays of 1486.6 eV energy, the X-rays can then remove electrons from any of carbon's three electron orbitals (1s, 2s, or 2p). Figure 3-8 shows the binding energy's' of the carbon atom and the removal of a 1s electron by an X-ray. Upon removal of the 1s electron, a detector measures the  $KE$  of the electron. The  $BE$  can then be calculated from the difference between the energy of the X-ray and the measured  $KE$  [Bru92].

In addition to obtaining elemental information from a sample, XPS can also be used to obtain bonding information. When an atom in a sample is in different chemical environments, then the measured kinetic energies from the atom can vary by a few eV. This produces a shift in the *BE* peaks. From these peak shifts, information is obtained as to which chemical environments the atom is present [Bru92]. For example, when a zinc atom is bonded to another zinc atom, the *BE* of the Zn 2p<sub>3,2</sub> photoelectron is 1021.8 eV. However, when a zinc atom is bonded to an oxygen atom, the *BE* is shifted to 1022.1 eV [Der92]. This shift is attributed to the change in how tightly the electron is bound to the zinc atom. When zinc is bonded with oxygen, the electron is bound more tightly to the zinc atom since the oxygen atom is more electronegative than zinc atom leaving the zinc atom with a higher positive charge.

### **Residual Gas Analysis**

Residual gas spectra were collected using a Dycor LC 200AMU series mass spectrometer from Ametek. These spectra were collected before and after each CL degradation experiment. A schematic of the residual gas analyzer is shown in Figure 3-9.

The RGA measures the mass to charge ratio of particular ions to determine their partial pressure in the vacuum chamber. It is comprised of an ion source, a quadrupole separation system and an ion detector, which are shown in Figure 3-9. In the ion source, a tungsten filament is heated, which produces electrons through thermionic emission, and when gas molecules enter the ion source and collide with the electrons, they become ionized. The ions are then focused into the quadrupole separation system, which is comprised of four rod like electrodes as shown in Figure 3-9. Then by applying a positive DC and RF voltage to one set of opposing electrodes and a negative DC and RF



voltage to the remaining pair, a complex time-dependent electric field is produced in the area within the four electrodes [Lar02]. By controlling the voltages on the electrodes, the passage of ions with a specific mass to charge ratio can be controlled and measured by a Faraday Cup detector or an electron multiplier which allows partial pressure detection down to  $10^{-13}$  Torr [Cha98].

#### Four Point Probe

A Jandel RM2 Four Point Probe was used to obtain the resistivity of ZnO:Al thin films grown on silicon wafers by pulsed laser ablation. The sample was placed on the sample stage. Then a four-point metal-tip probe assembly was lightly pressed onto the surface as shown in Figure 3-10. The outer probes are connected to the current source, and the inner probes detect the voltage drop. The sheet resistance is given by:

$$R_s = \frac{K \cdot V}{I}, \quad (3-2)$$

where  $K$  is a constant dependent on the configuration and spacing of the contacts. Since the samples were large compared to the probe assembly and the probe spacing was large compared with the films thickness, then the  $K$  value equals  $\pi/\ln 2$  or 4.53 [Ohr92].

Once the sheet resistance is calculated and the thickness of the thin film is known, then the resistivity of the film can be calculated using the following equation:

$$R_s = \frac{\rho}{t}, \quad (3-3)$$

where  $\rho$  is the resistivity of the film and  $t$  is the film thickness [May00].

#### UV-VIS

A Perkin Elmer Lambda 800/900 UV-VIS was used to measure the transmittance of aluminum doped zinc oxide thin films. These films were grown on Coming 1737 glass.

The thin films were analyzed using a double beam set up in transmission mode from 250 nm to 800 nm.

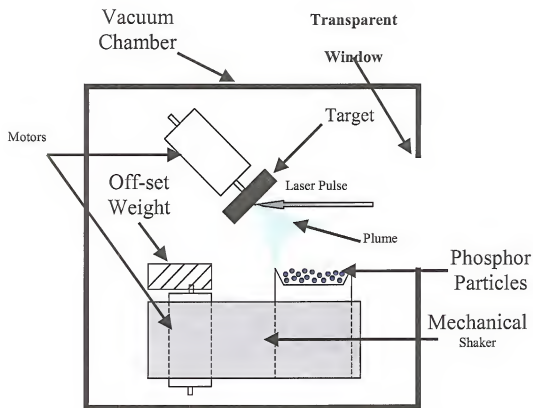


Figure 3-1. A schematic of the modified pulsed laser deposition used for particle coatings.

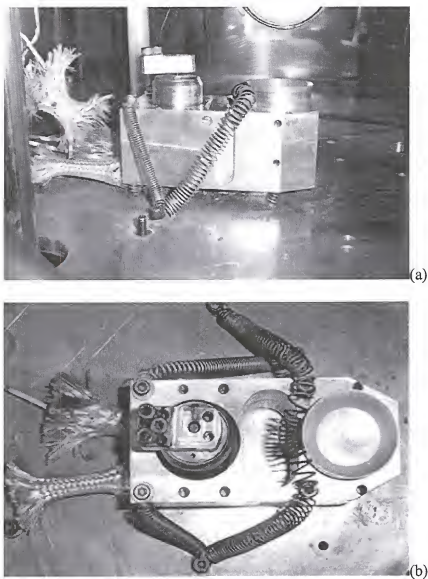


Figure 3-2a,b. Picture of mechanical shaker used for particle fluidization. (a) Picture of side view of the mechanical shaker and (b) Picture of top view of the mechanical shaker.

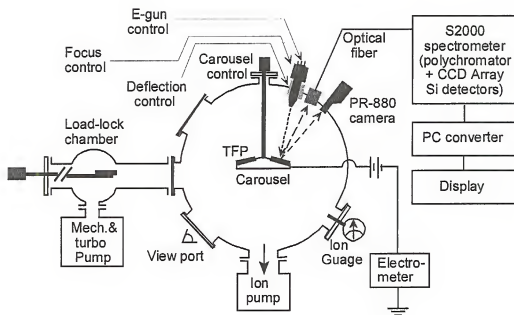


Figure 3-3. Schematic illustration of the CL measurement system for degradation experiments [Gon00].

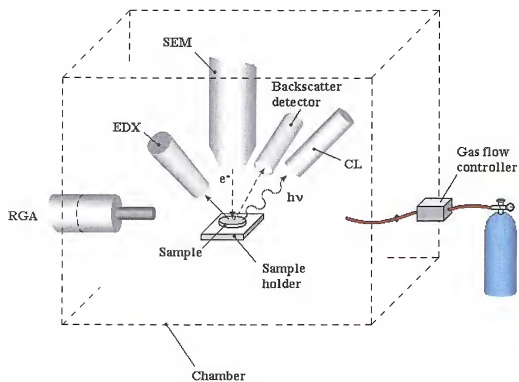


Figure 3-4. Schematic illustration of CL system used in conjunction with a JEOL 6400 SEM.

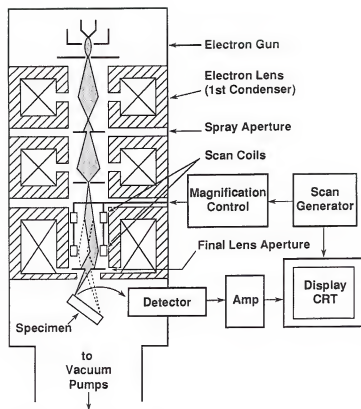


Figure 3-5. A schematic illustration showing a cross-sectional view of a typical SEM electron column, deflection system, and electron detectors [Gol92].

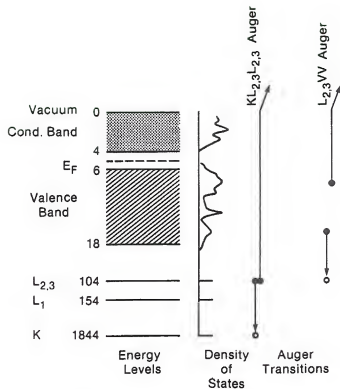


Figure 3-6. Energy level diagram of solid Si, including the density of states of the valence and conduction bands, a schematic representation of the Si KL<sub>2,3</sub>L<sub>2,3</sub> Auger transitions, and a subsequent LVV Auger transition [Bru92].



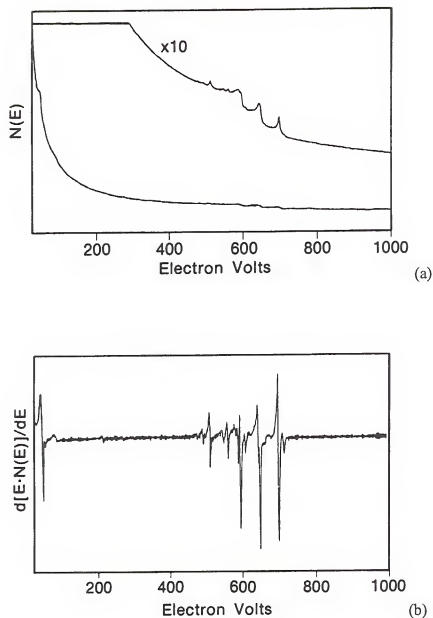


Figure 3-7a,b. These figures show two different forms of the secondary electron energy spectra from a slightly contaminated Fe surface. (a). Shows the directly acquired data, and (b) shows a subsequently mathematically derived spectra that allows for improved signal-to-noise ratio in the raw data [Bru92].

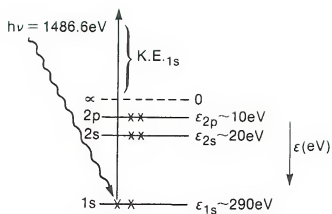


Figure 3-8. Schematic representation of the electronic energy levels of a carbon atom and the photoionization of a carbon 1s electron [Bru92].

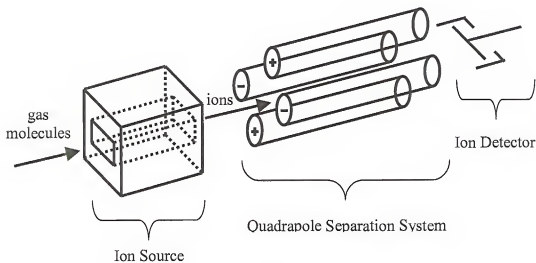


Figure 3-9. Shows a schematic of a residual gas analyzer. It is comprised of an ion source, a quadrupole separation system and an ion detector.

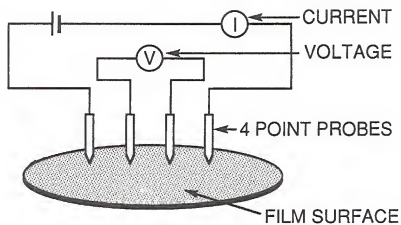


Figure 3-10. Schematic setup of a four-point probe method for measuring sheet resistance [Ohr92].

## CHAPTER 4 EFFECT OF ITO COATINGS ON ZNS:AG ON CL DEGRADATION

### Introduction

This chapter presents results studying the effect that coating ZnS:Ag with a nanometer thick layer of indium tin oxide has on the phosphor's cathodoluminescent lifetime, as well as, the effect of partial pressure of water on the cathodoluminescent degradation lifetime. The effect of partial pressure of water is discussed in two categories: low water partial pressure ( $1 \cdot 10^{-7}$  Torr) and high water partial pressure ( $6.1 \cdot 10^{-7}$  Torr).

The CL results in this were obtained using the CL system described in Figure 3-3. The two different partial pressures of water were achieved by throttling the poppet valve shown on the CL system in Figure 3-3. By partially closing the poppet valve, the ion pumping speed could be controlled in order to achieve the desired partial pressure of water. In both vacuum conditions, the partial pressure of water dominated the total background pressure.

### Background

As discussed in Chapter 2, the results reported by Swart et al. [Swa96, Swa99], Holloway et al. [Hol96, Hol00], etc. [Seb95, Tro96, Oos97] showed the formation of a non-luminescent oxide layer on the surface of the phosphor degradation. It was also shown that vacuum ambients with high concentrations of water or oxygen increased the rate of degradation or oxide layer growth. The current studies were intended to show the reduction in degradation rate, as well as, the adverse affects that high partial pressures of water have on uncoated and coated ZnS:Ag.

## Results and Discussion

### Indium Tin Oxide – Coated ZnS:Ag

The Osram Sylvania ZnS:Ag phosphor particles were coated using a modified laser ablation technique that was described in Chapter 3. 2.0g of ZnS:Ag phosphor particles was coated with indium tin oxide (ITO) at a pressure of  $5 \cdot 10^{-5}$  mTorr, a laser fluence of  $1.5 \text{ J/cm}^2$ , for 24,000 pulses (30 min at 20 Hz). The coated samples were then analyzed using Auger Electron Spectroscopy (AES) to show the presence of the ITO coating on the ZnS:Ag surface. Figure 4-1a,b shows two AES spectra, where the spectrum in Figure 4-1a was obtained from a one-micron diameter area on the surface of a particle and the spectrum in Figure 4-1b was obtained from an approximate area of  $\sim 100 \text{ }\mu\text{m}$  including numerous particles. By obtaining similar results from the small and large areas, one can infer that the amount of ITO deposited on the particles was quite uniform. However, it was not possible to analyze the exact chemical composition of the coatings because of charging, especially in the uncoated ZnS:Ag.

The coated and uncoated samples were then degraded at a vacuum pressure of  $6.1 \cdot 10^{-7}$  Torr using an accelerating voltage of 5 keV with a beam diameter of 0.15 mm. The electron current density was kept constant during the degradation experiment at  $2.0 \text{ }\mu\text{A/cm}^2$ . The results of the degradation experiments are shown in Figure 4-2. As one can see, the presence of the ITO coating has dramatically improved the degradation lifetime of the ZnS:Ag. The intensity of the coated sample only decreased by about 30% during the CL degradation, whereas the uncoated sample intensity reduced by about 80% after  $\sim 5 \text{ C/cm}^2$ .

The particle surface of the uncoated and the ITO coated ZnS:Ag particles were then analyzed using X-ray photoelectron spectroscopy (XPS) before and after being

irradiated with an electron beam. However, since the XPS (PHI 5100) has a poor lateral resolution ( $\sim 1$  cm by  $\sim 1$  cm) and the electron beam during the CL degradation has a diameter of 0.15 mm, the electron beam had to be rastered across the sample to obtain an area large enough to be analyzed. In order to ensure that the information obtained from the electron beam irradiated samples was coming solely from the irradiated region, gold foil was used as a mask to cover the sample leaving only the electron beam irradiated region exposed. Initially, the phosphor surface was sputter cleaned for two minutes with an  $\text{Ar}^+$  beam to partially remove the surface contamination.

XPS analysis was used to characterize the chemical states of Zn, S, C, and O atoms on the ZnS:Ag particles. The XPS spectra results for the Zn  $2p_{3/2}$  peak, corresponding to the Zn-S bond, and the S 2p peak, corresponding to S-Zn bond, of the Osram Sylvania, uncoated and coated ZnS:Ag samples are shown in Figures 4-3 and 4-4. Figures 4-3a,b,c show the XPS results of the Zn  $2p_{3/2}$  peak for the Osram Sylvania ZnS:Ag powder, the electron beam irradiated ZnS:Ag sample coated with ITO, and the electron beam irradiated uncoated ZnS:Ag powder, respectively. From this figure, one can see that the binding energy of the Zn  $2p_{3/2}$  peak of the commercial ZnS:Ag is located at 1022.1 eV, which is in excellent agreement with a recent published value of 1022.0 eV [Der92]. In Figure 4-3b, the XPS spectrum shows that there are two components to the Zn peak. The deconvolution of the acquired peak shows that it is comprised of a peak similar to that found in the original powder and a peak that is at a higher binding energy. The shift to a higher binding energy is most likely attributed to the oxidation of Zn in ZnS. The increase in binding energy due to oxidation is caused by the higher positive charge associated with a zinc atom bonded to oxygen than sulfur (oxygen is more electro-

negative) [Bru92]. This causes the measured kinetic energy to decrease, therefore increasing the binding energy. For the uncoated ZnS:Ag (Figure 4-3c), the Zn  $2p_{3/2}$  peak corresponding to ZnS has completely disappeared and only a contaminated peak located at a higher binding energy remains. Again this contaminated peak can be attributed to an oxide (or sulfate compound).

Figures 4-4a,b,c show the XPS results of the S 2p peaks for Osram Sylvania ZnS:Ag powder, the electron beam irradiated ZnS:Ag sample coated with ITO, and the electron beam irradiated commercially available ZnS:Ag particulates, respectively. The S 2p spectrum of ZnS is known to contain the S  $2p_{3/2}$  and S  $2p_{1/2}$  spin-orbit doublet, which is separated by 1.2 eV with an intensity ratio of 2:1. As one can see in Figure 4-4a, the binding energy of S  $2p_{3/2}$  was 161.8 eV, which agrees very well with published data for ZnS [Der92]. The second peak seen in Figure 4-4a, presumably belonging to S  $2p_{1/2}$  is, however, located at a higher binding energy than the usual 1.2 eV difference and its intensity is significantly lower than half of the S  $2p_{3/2}$  peak intensity. This indicates the presence of a surface contamination layer even in the commercially available phosphor particles, which cannot be removed by 2 minutes of  $Ar^+$  sputtering. It was also observed that prolonged  $Ar^+$  sputtering leads to preferential S loss. A comparison of the XPS spectra shown in Figures 4-4b and 4-4c with that of the commercially available particles (Figure 4-4a) indicates that after electron beam irradiation, the position of the S 2p peak shifts towards a higher binding energy. However, for the electron beam irradiated powder that was coated with an ITO film, the S  $2p_{3/2}$  peak that is located at 161.8 eV, the position corresponding to S-Zn bond, is clearly visible, while there is no such peak for the uncoated phosphor powder (see Fig. 4c). From the lack of the S  $2p_{3/2}$

peak corresponding to the S-Zn bond in Figure 4-4 (c) and an estimated electron inelastic mean free path of  $\sim 15 \text{ \AA}$ , it can be inferred that the oxidized dead layer formed on the surface of the phosphor particles is at least  $50 \text{ \AA}$  thick [Gao00]. In addition, the Auger parameter estimated for Zn for the electron beam irradiated and coated powder was around  $2111.0 \text{ eV}$ , which is almost identical with previous reports for ZnS and differs from the  $2102.2 \text{ eV}$  value for ZnO reported in literature [Lak95, Fut98].

The XPS results shown in Figures 4-3 and 4-4 clearly demonstrated that by applying a nano-meter scale ITO coating to the ZnS:Ag phosphor, the cathodoluminescent degradation can be dramatically reduced. The coated ZnS:Ag samples only lost 30% of its brightness after exposure to an electron (coulombic) dose of  $5 \text{ C/cm}^2$  as compared to the uncoated ZnS:Ag, where 80% of its initial brightness was lost. The difference in these degradation curves was shown to be the retardation of the formation of the non-luminescent layer.

#### **Effect of the Partial Pressure of Water on CL Degradation**

Uncoated and the ITO coated ZnS:Ag were degraded at two different vacuum levels where the partial pressure of water dominated the vacuum level. The first set of degradation experiments were performed at a total vacuum pressure of  $6.1 \cdot 10^{-7} \text{ Torr}$  (high water partial pressure). The results of which were presented in the previous section (Figures 4-2 – 4-4). The second pressure level used in this study was  $1 \cdot 10^{-7} \text{ Torr}$  (low water partial pressure). Figure 4-5 shows a comparison of the residual gas analysis (RGA) spectra for the two vacuum conditions. As seen in Figure 4-5, the predominant difference in the two vacuum conditions was the amount of  $\text{H}_2\text{O}$  species present.

By degrading ZnS:Ag at these two different vacuum levels, the effect of water species on CL lifetime can be determined. Figure 4-6 shows the CL degradation curves



for the phosphors degraded at  $1 \cdot 10^{-7}$  Torr (low water vapor case) while maintaining all other conditions (beam energy, current density, and beam diameter). In this case, as was seen previously for the high water case, the coated sample degraded slower than the uncoated sample. At an electron dose of  $25 \text{ C/cm}^2$ , the ITO coated ZnS:Ag has maintained ~60 % of its initial brightness while the uncoated ZnS:Ag only maintained ~30 % of its initial brightness. However, notice that in this low water vapor pressure case, the phosphors were degraded out to an electron dose of  $25 \text{ C/cm}^2$  as compared to the earlier case of  $5 \text{ C/cm}^2$ .

These results show that to obtain longer phosphor lifetimes, it is advantageous to not only have a nano-encapsulating ITO layer on the phosphor, but to also maintain a high vacuum level during electron beam irradiation with minimal water vapor present. By applying the coating to the phosphor surface, the XPS data showed (Figures 4-3 and 4-4) that the electron beam stimulated surface chemical reactions were slowed. The ITO layer prevented the harmful water molecules from adsorbing directly on the phosphor surface, which could then be dissociated into atomic oxygen and hydrogen with the oxygen reacting with the Zn in ZnS:Ag forming a ZnO non-luminescent layer. The negative effect of the high water vapor was also shown where an increase in the partial pressure of water increased the degradation rate. This result agrees with Equation 2-22 developed by Holloway et al. [Hol00] in which an increase in partial pressure of molecular gas in the vacuum causes a higher rate of S lost from the surface and therefore, a decrease in CL brightness.

In addition to performing CL degradation experiments, CL spectra were taken of the uncoated and coated samples. A comparison the two CL spectra are shown in Figure

4-7. This figure shows that the ITO coating does not affect change the CL emission spectra of the ZnS:Ag. This is important for industry that the phosphors still emit light in the desired wavelength.

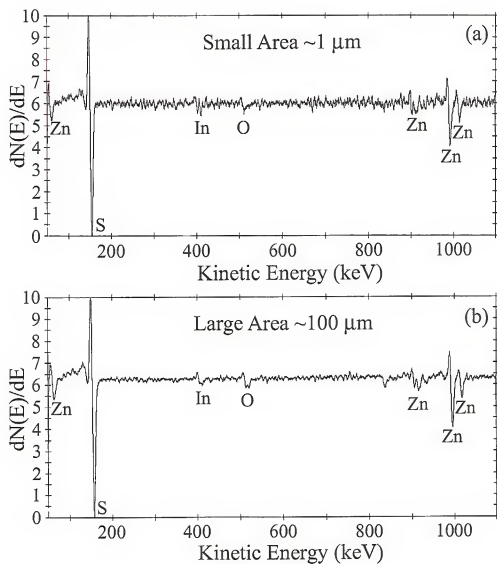


Figure 4-1 a,b. Auger electron spectroscopy spectra of indium tin oxide coated ZnS:Ag.  
(a) AES spectra of  $\sim 1 \mu\text{m}$  area. (b) AES spectra of  $\sim 100 \mu\text{m}$  area.

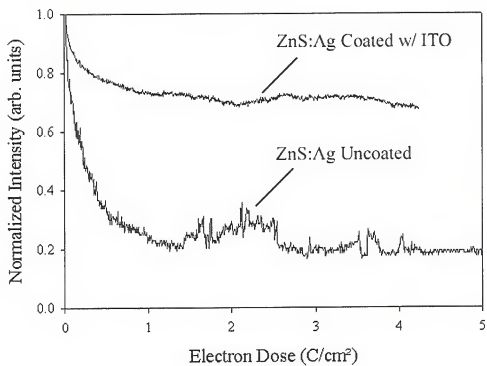


Figure 4-2. Cathodoluminescence degradation curves for commercial ZnS:Ag and ZnS:Ag coated with indium tin oxide at  $6.1 \times 10^{-7}$  Torr.

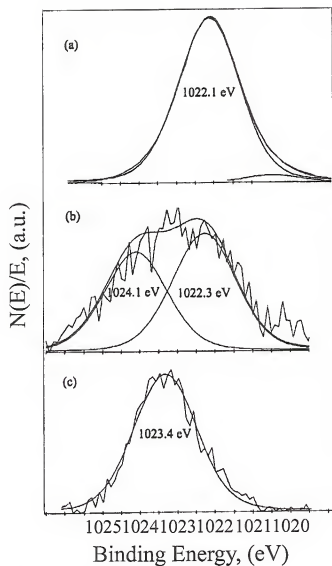


Figure 4-3. X-ray photoelectron spectroscopy results of the Zn  $2p_{3/2}$  peak for (a) the commercial ZnS:Ag powder, (b) the electron beam irradiated ZnS:Ag sample coated with indium tin oxide, and (c) the electron beam irradiated uncoated ZnS:Ag powder.

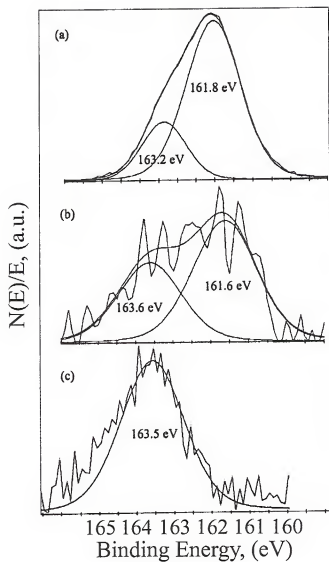


Figure 4-4. X-ray photoelectron spectroscopy results of the S 2p peak for (a) the commercial ZnS:Ag powder, (b) the electron beam irradiated ZnS:Ag sample coated with indium tin oxide, and (c) the electron beam irradiated uncoated ZnS:Ag powder.

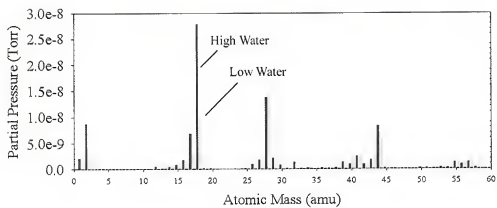


Figure 4-5. RGA spectra of the high and low water partial pressures used during CL degradation.

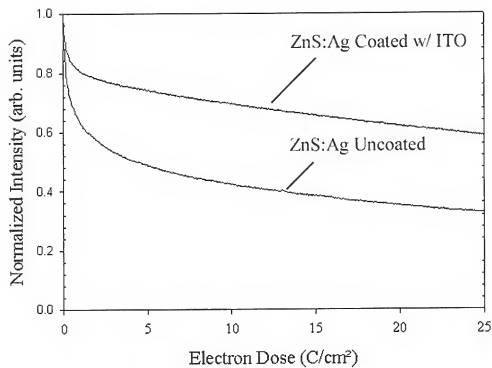


Figure 4-6. Cathodoluminescence degradation curves for commercial ZnS:Ag and ZnS:Ag coated with indium tin oxide at  $1 \times 10^{-7}$  Torr.



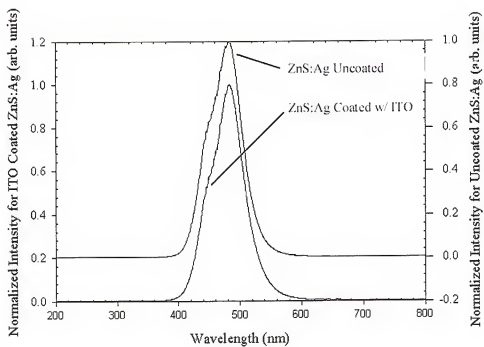


Figure 4-7. CL spectra comparison of coated and uncoated ZnS:Ag.

## CHAPTER 5

### EFFECT OF OXYGEN PARTIAL PRESSURE DURING ZAO GROWTH ON CL DEGRADATION OF ZNS:AG

This chapter presents the results of the studies showing the effect of oxygen deposition pressure on aluminum-doped zinc oxide (ZAO) coatings as they pertain to the cathodoluminescent (CL) degradation of ZnS:Ag. ZAO was deposited onto ZnS:Ag at three different oxygen deposition pressures: 100 mTorr, 0.6 mTorr, and 0.14 mTorr. The ZAO coated ZnS:Ag phosphors were then degraded at a vacuum of  $5.0 \cdot 10^{-5}$  Torr in the modified SEM (JEOL 6400) described in Chapter 3.

First, ZAO was deposited onto Si (100) wafers at the three oxygen deposition pressures. This was done in order to obtain film thicknesses, as well as, electrical and optical properties of ZAO. The film thickness was measured using an Alpha Step Profilometer and the resistivity was obtained from four-point probe measurements. The results are listed in Table 5-1. In order to obtain transmittance values of these films, the ZAO films were deposited onto Corning 1737 glass. The transmittance values of these films were then measured using a spectrophotometer. The resulting optical spectra are shown in Figure 5-1 and the percent transmittance was also included into Table 5-1. Then from Table 5-1 one can see that by depositing ZAO at these three varying oxygen deposition pressures, three distinct cases arise. These conditions are: (1) high optical transmittance and low electrical conductivity, (2) high optical transmittance and high electrical conductivity, and (3) low optical transmittance and high electrical conductivity.

Table 5-1. This table lists the ZAO film thickness, ZAO film resistivity, and ZAO transmittance at 100 mTorr, 0.6 mTorr, and 0.14 mTorr.

Deposition Pressure	Thickness	Resistivity, $\rho$	Ave. Transmittance at 500 nm
100 mTorr	4581	$0.314 \Omega\cdot\text{cm}$	91.4 %
0.6 mTorr	3004	$8.9\cdot 10^{-4} \Omega\cdot\text{cm}$	80.9 %
0.14 mTorr	4280	$2.2\cdot 10^{-3} \Omega\cdot\text{cm}$	0 %

The three different pressure conditions were then used during the deposition of ZAO on ZnS:Ag. However, to ensure that the coatings at the three different pressures were similar in thickness, growth rates were obtained by depositing ZAO on Si wafers at each of the pressures and then measuring the thickness with x-ray reflectometry (XRR). The results of the film thicknesses and growth rates are listed in Table 5-2.

Table 5-2. This table lists the growth rate of ZAO at 100 mTorr, 0.6 mTorr, and 0.14 mTorr.

Deposition Pressure	Number of Pulses	ZAO Thickness	Growth Rate
100 mTorr	703	632.511	0.703 /pulse
0.6 mTorr	727	511.25	0.900 /pulse
0.14 mTorr	529	499.796	0.945 /pulse

After the ZnS:Ag phosphors were coated with ZAO at the three different deposition pressures, they were degraded. The resulting CL degradation curves are shown in Figure 5-2. From this figure, one can see that all three coated ZnS:Ag phosphors have longer CL lifetimes in comparison to the uncoated ZnS:Ag phosphor. From the three coated samples, the phosphor coated with a ZAO film at 0.14 mTorr had the longest CL

degradation life time, followed by 100 mTorr, and 0.6 mTorr. However, these results were quite unexpected. It was hypothesized that the ZnS:Ag that was coated with ZAO at an oxygen deposition pressure of 0.6 mTorr would result in the longest CL degradation lifetime. At this pressure, it was thought that the conducting nature of the film would reduce the charge accumulation on the surface of the phosphor, which would reduce the surface potential and increase the kinetic energy of the primary electrons during CL degradation. In addition, the reduction of surface charging was also believed to aid in the reduction of band bending effects [Swa99, Swa00, Hol99] where there would be an increased probability of recombination of electron-hole pairs. The high optical transmittance in the visible spectrum of the ZAO films deposited at an oxygen pressure of 0.6 mTorr was initially thought to reduce the impedance of the coating to the photons being generated in the phosphor powder.

These unexpected results showed that the electrical and optical properties of the ZAO coating were not the dominating factors in controlling the reduction of CL degradation. As seen in Figure 5-2, the CL degradation of the ZAO coated ZnS:Ag phosphor seems to occur at two different rates. The phosphors coated with ZAO at an oxygen deposition pressure of 100 mTorr and 0.6 mTorr lose their brightness at a much faster rate than the phosphors coated at 0.14 mTorr. To determine the cause of the changes in the CL degradation, ZAO thin films, approximately 300 nm thick, were deposited on silicon (100) wafers. The deposited ZAO thin films were then degraded and analyzed using XPS and compared to the undegraded ZAO thin films.

XPS analysis was used to characterize the chemical states of Zn, O, and C in the ZAO thin films. The peak positions of the Zn  $2p_{3/2}$  peaks before and after degradation are

listed in Table 5-3. From this table, one can see that the as the oxygen deposition pressure decreases, the Zn 2p<sub>3/2</sub> peak shifts to smaller binding energies. This corresponds to the lower oxygen content in the ZAO thin films deposited at the lower oxygen pressures. After degradation, the Zn 2p peak shifts to higher binding energies at each of the deposition pressures. This shift to higher energies indicates that the Zn 2p peak has become further oxidized. However, at 0.14 mTorr, the shift is significantly larger than at the other two deposition pressures. The shift in the Zn 2p spectra for the three oxygen deposition pressures is shown in Figure 5-3. This dramatic increase in binding energy shows that the oxygen deficient ZAO thin film is more reactive than the two other deposition conditions. This higher reactivity could be responsible for the increased degradation lifetime. The coating deposited at 0.14 mTorr acts not only as a protective barrier for the phosphor surface, but also as a chemical barrier where the coating behaves as a scavenger material (or a getter material) and reacts with the harmful atomic species which would normally react with the phosphor surface.

Table 5-3. This table lists the Zn 2p peak values before and after CL degradation.

Deposition Pressure	Zn 2p Before Degradation	Zn 2p Before Degradation
100 mTorr	1020.73 eV	1020.88 eV
0.6 mTorr	1020.62 eV	1021.0 eV
0.14 mTorr	1020.52 eV	1021.2 eV

The proposed mechanism for this improved CL degradation is based on electron beam stimulated surface chemical reactions (ESSCR) [Seb95, Hol99, Hol00, Swa00], where instead of the harmful residual gases (H<sub>2</sub>O, O<sub>2</sub>, H<sub>2</sub>) reacting with the phosphor surface,

the ZAO coating is being attacked. The ZAO film deposited at 0.14 mTorr is highly deficient in oxygen causing the ZAO film to have a higher metallic zinc phase. Since this film is rich in zinc, it is susceptible to oxidation from the oxygen containing species present in the residual gases. From residual gas analysis (RGA), it was found that  $H_2O$  molecules were the dominant molecular species present during the CL degradation experiments. The RGA results for all the degradation experiments are shown in Figure 5-4. This figure shows that the residual gases were similar in all three CL degradation experiments. As the water molecules come in contact with the electron beam, the water molecules are dissociated and the reactive atomic oxygen reacts with the zinc in the coating to form zinc oxide. The possible reactions for this mechanism are:



The reaction of the reactive atomic oxygen with the available zinc incorporates the detrimental oxygen into the coating material. In essence, eliminating the possibility that the reactive atomic oxygen can react with the phosphor surface. Through this reaction mechanism, the oxygen depleted ZAO film deposited at 0.14 mTorr behaves as a scavenger material and therefore protects the phosphor from rapid CL brightness loss. However, once the oxygen deficient coating becomes fully oxidized, the phosphor will begin to degrade at a higher rate.

In addition to being more reactive, the ZAO deposited at 0.14 mTorr also showed to have a better conformal coverage than the other two coatings. Figures 5-5a,b and 5-6a,b show TEM micrographs at two different magnification levels of ZnS:Ag coated with ZAO deposited at 0.6 mTorr and 0.14 mTorr. From these two sets of figures, one can see

that the ZnS:Ag phosphor particles coated at 0.14 mTorr is coated more uniformly with smaller particles than the phosphor particles coated at 0.6 mTorr. The ZAO coating deposited at 0.14 mTorr is comprised of two distinctly different sizes of nanoclusters. The coating is dominated by nanoclusters of approximately 10 nm in size which provides a continuous coating on the ZnS:Ag surface and on top of this layer, a few sparsely distributed larger sized nanoclusters of approximately 120 nm in size. The ZAO coating deposited at 0.6 mTorr is a non-continuous coating where the nanocluster sizes range from 80-120 nm. This difference in coating uniformity could also be responsible for the increased CL degradation lifetime. The continuous coating on the ZnS:Ag phosphors coated at 0.14 mTorr provides better protection of the phosphor surface from the harmful residual gases. The exposed areas of the particles in the 0.6 mTorr case are more readily attacked by ESSCR and therefore degrade faster than the 0.14 mTorr case.

In addition to CL and TEM experiments, SEM and CL images were taken before and after each of the phosphors were degraded. This was also done for the ZAO films that were grown on silicon wafers. In comparing Figures 5-7a,b and 5-8a,b one can see that the uncoated SEM image (Figure 5-7a) showed charging effects from the striations/distortions in the SEM image which are missing from the SEM image in Figure 5-8b. This agrees with the predicted ESSCR where the ZnS:Ag is attacked by the oxygen containing residual gases forming a non-luminescent layer of ZnO. The lack of charging in the after degradation micrograph indicates that this more conductive ZnO layer has formed. Then comparing the CL images in Figures 5-7b and 5-8b, one can see that the top layer of phosphor particles has lost significant brightness. This can be seen by looking at the change in contrast between the before and after images. When looking at

the before case, the particles have essentially the identical brightness and there is very little difference in the contrast of the CL image. Then in the after degradation case, the top layer of phosphors appear dimmer or show less intensity as compared to the phosphors buried beneath the top layer. This shows that the top layer, which was directly in contact with the electron beam, degraded much faster than the underlying phosphors that were somewhat, shielded.

Figures 5-9a,b and 5-10a,b show the SEM and CL micrographs of ZnS:Ag coated with ZAO at an oxygen deposition pressure of 100 mTorr before and after CL degradation. In Figure 5-9a, the SEM image shows some charging effects which is expected due to the lower electrical conductivity value listed in Table 5-1. Again, as in the uncoated case, after the sample was degraded, the non-luminescent ZnO layer grew and reduced the charging effects. The CL images in Figures 5-9b and 5-10b show similar results to the uncoated case, where the top layer of the embedded phosphors are degraded at a faster rate than the phosphors located beneath this initial layer.

Figures 5-11a,b and 5-12a,b show the SEM and CL micrographs of ZnS:Ag coated with ZAO at an oxygen deposition pressure of 0.6 mTorr before and after CL degradation. In these before degraded samples, there was no observed charging in the SEM image which was expected due to the films high electrical conductivity at this deposition pressure (Table 5-1).

Figures 5-13a,b and 5-14a,b show the SEM and CL micrographs of ZnS:Ag coated with ZAO at an oxygen deposition pressure of 0.14 mTorr before and after CL degradation. Again in these figures show that the SEM images showed no signs of charging as with the 0.6 mTorr case. The CL images (Figures 5-13b and 5-14b) show



very little difference in the contrast of the particles before and after degradation. The reduced difference in the contrast in the CL images than the previous cases indicates that these coated phosphors degraded slower than the other coated phosphors which was shown in Figure 5-2.

Figure 5-15a,b shows the SEM and CL image of ZnS:Ag coated with ZAO at 0.6 mTorr after degradation at a lower magnification. These two figures were taken at a lower magnification. These figures show how detrimental the degradation of ZnS:Ag is compared to the non-degraded region.

Figure 5-16a,b shows the SEM images of ZAO deposited on a silicon wafer before and after degradation. Figure 5-16b shows that after degradation the ZAO thin film surface was altered. The darker color is due to carbon contamination. This carbon contamination was detected using XPS.

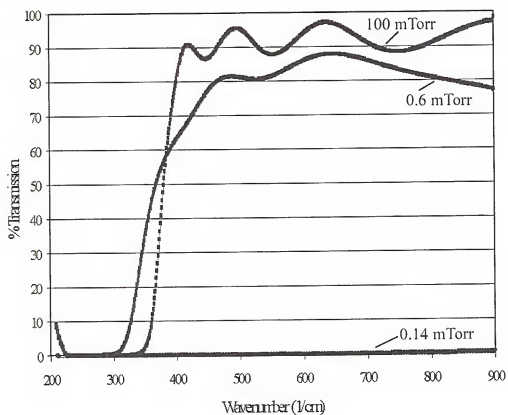


Figure 5-1. This figure shows the optical spectra of ZAO deposited on Si at UV-VIS data of ZAO films grown at 100 mTorr, 0.6 mTorr, and 0.14 mTorr.

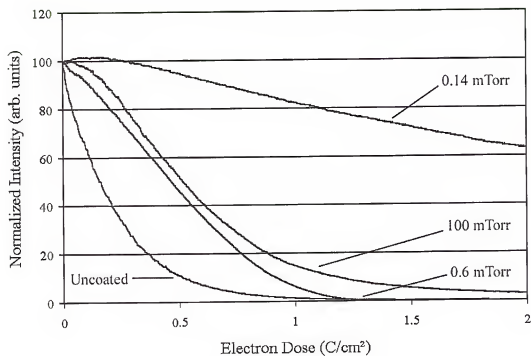


Figure 5-2. This figure shows the CL degradation curves of ZnS:Ag coated with ZAO at oxygen deposition pressures 100 mTorr, 0.6 mTorr, and 0.14 mTorr.

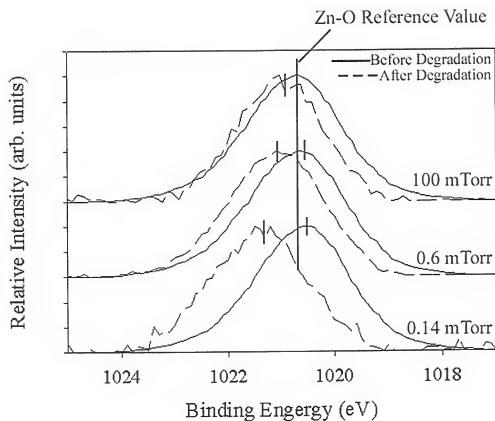


Figure 5-3. XPS results of Zn 2p peak of ZAO thin films deposited on silicon wafers at 100 mTorr, 0.6 mTorr, and 0.14 mTorr before and after degradation.

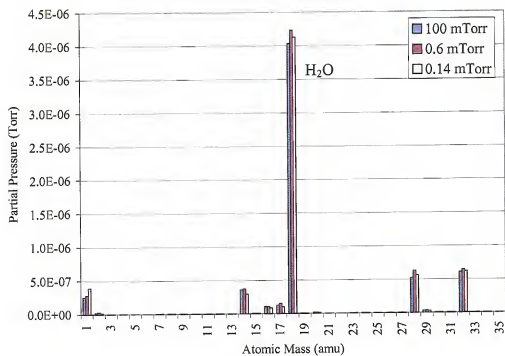


Figure 5-4. RGA spectra taken during CL degradation experiments of ZnS:Ag coated with ZAO at 100 mTorr, 0.6 mTorr, and 0.14 mTorr.

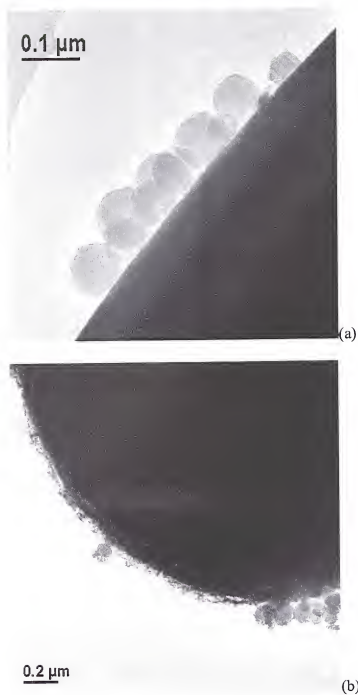


Figure 5-5a,b. TEM micrographs of ZnS:Ag particles coated with ZAO. (a). TEM micrograph showing ZAO coating on ZnS:Ag at a oxygen deposition pressure of 0.6 mTorr. (b). TEM micrograph showing ZAO coating on ZnS:Ag at a oxygen deposition pressure of 0.6 mTorr.

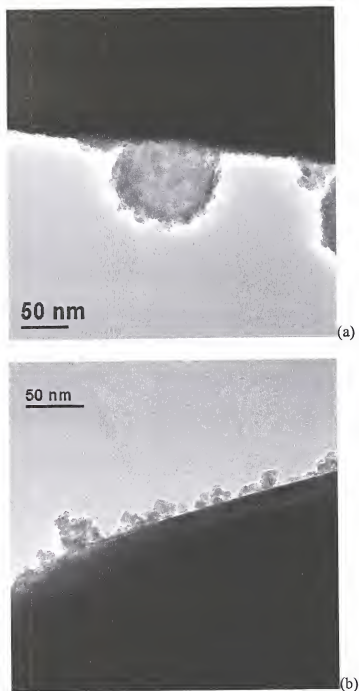


Figure 5-6a,b. TEM micrographs of ZnS:Ag particles coated with ZAO. (a). TEM micrograph showing ZAO coating on ZnS:Ag at a oxygen deposition pressure of 0.6 mTorr. (b). TEM micrograph showing ZAO coating on ZnS:Ag at a oxygen deposition pressure of 0.6 mTorr.

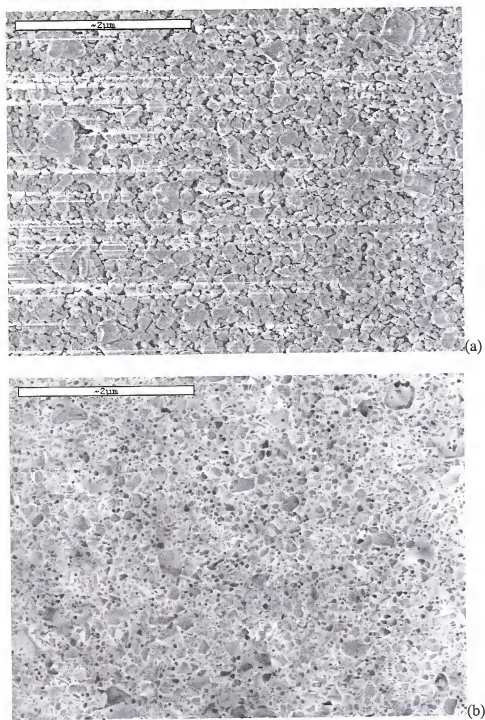


Figure 5-7a,b. Micrographs of uncoated ZnS:Ag before degradation. (a) SEM micrograph of ZnS:Ag before degradation. (b) CL micrograph of ZnS:Ag before degradation.



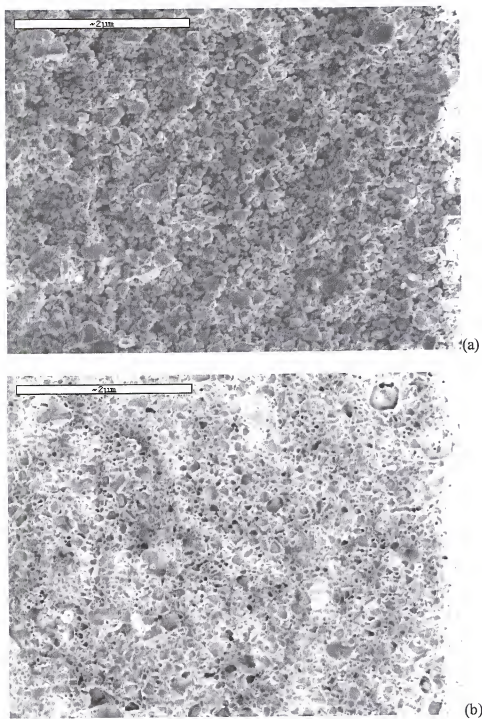


Figure 5-8a,b. Micrographs of uncoated ZnS:Ag after degradation. (a) SEM micrograph of ZnS:Ag after degradation. (b) CL micrograph of ZnS:Ag after degradation.

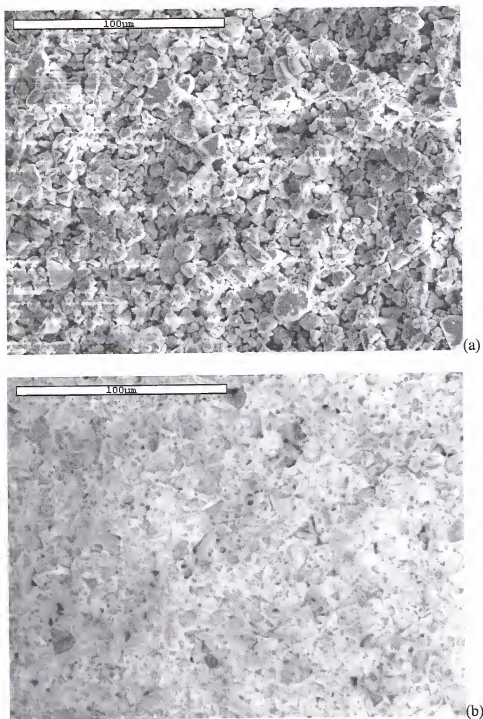


Figure 5-9. Micrographs of ZnS:Ag coated with ZAO at 100 mTorr before degradation. (a) SEM micrograph of ZnS:Ag coated with ZAO before degradation. (b) CL micrograph of ZnS:Ag coated with ZAO before degradation.

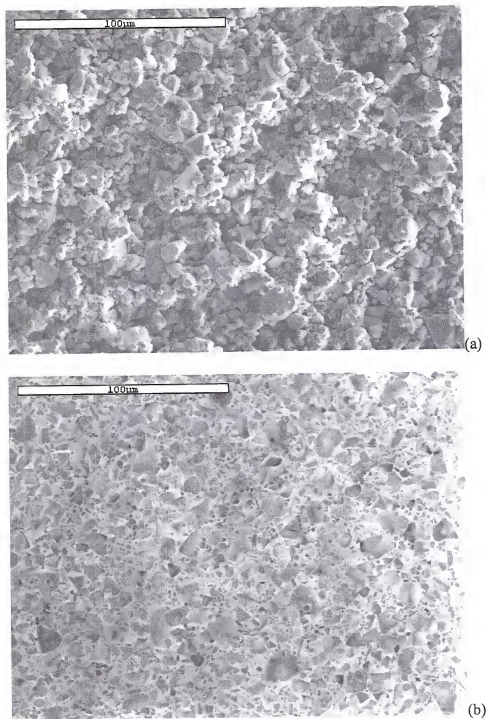


Figure 5-10a,b. Micrographs of ZnS:Ag coated with ZAO at 100 mTorr after degradation. (a) SEM micrograph of ZnS:Ag coated with ZAO after degradation. (b) CL micrograph of ZnS:Ag coated with ZAO after degradation.

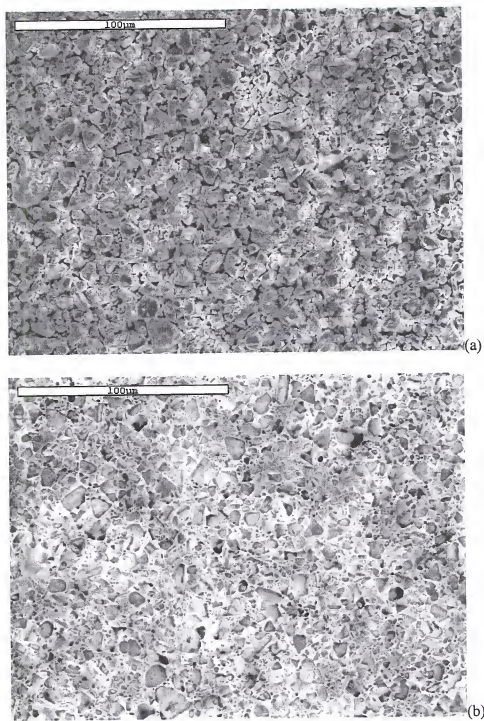


Figure 5-11a,b. Micrographs of ZnS:Ag coated with ZAO at 0.6 mTorr before degradation. (a) SEM micrograph of ZnS:Ag coated with ZAO before degradation. (b) CL micrograph of ZnS:Ag coated with ZAO before degradation.

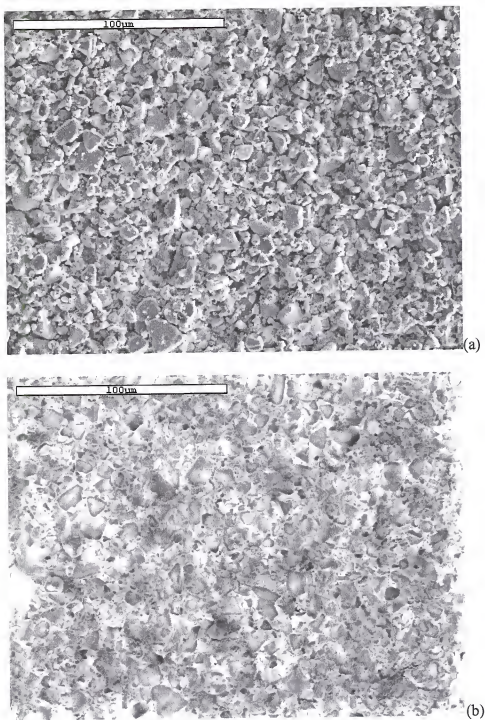


Figure 5-12a,b. Micrographs of ZnS:Ag coated with ZAO at 0.6 mTorr after degradation. (a) SEM micrograph of ZnS:Ag coated with ZAO after degradation. (b) CL micrograph of ZnS:Ag coated with ZAO after degradation.



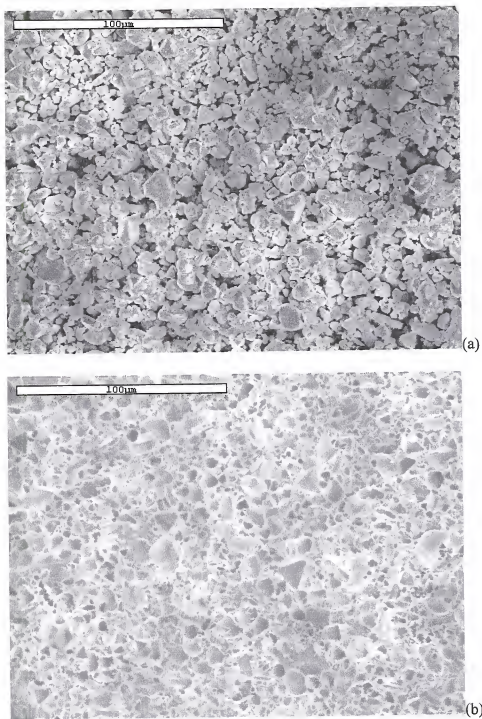


Figure 5-13a,b. Micrographs of ZnS:Ag coated with ZAO at 0.14 mTorr before degradation. (a) SEM micrograph of ZnS:Ag coated with ZAO before degradation. (b) CL micrograph of ZnS:Ag coated with ZAO before degradation.

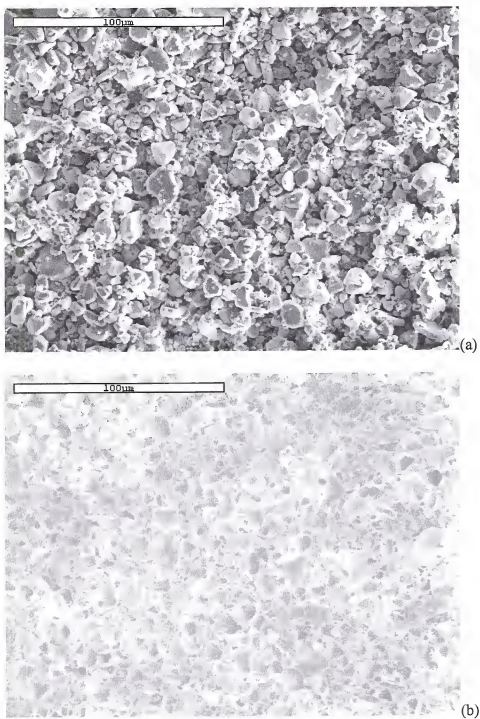


Figure 5-14a,b. Micrographs of ZnS:Ag coated with ZAO at 0.14 mTorr after degradation. (a) SEM micrograph of ZnS:Ag coated with ZAO after degradation. (b) CL micrograph of ZnS:Ag coated with ZAO after degradation.

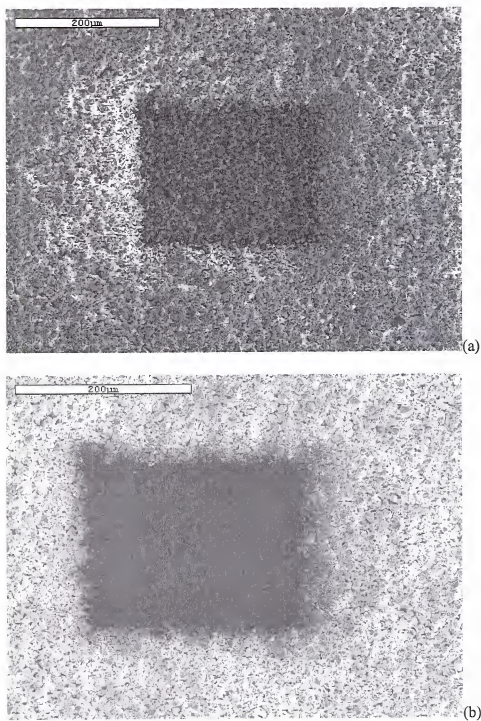


Figure 5-15a,b. Micrographs of ZnS:Ag coated with ZAO at 0.6 mTorr showing the degraded region after degradation. (a) SEM micrograph of ZnS:Ag coated with ZAO after degradation. (b) CL micrograph of ZnS:Ag coated with ZAO after degradation.



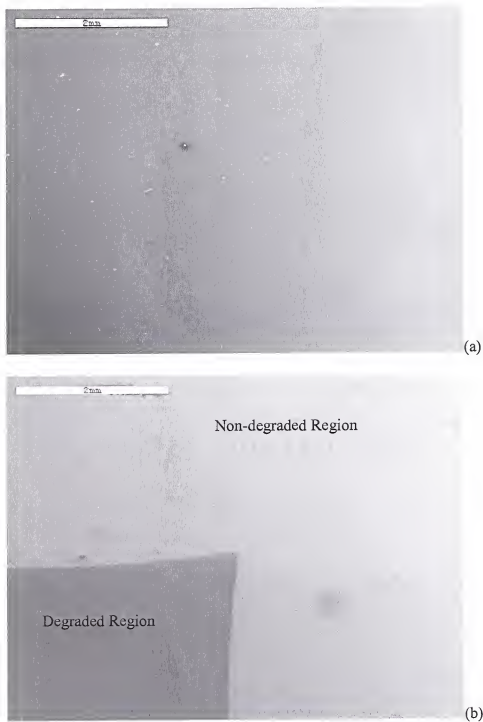


Figure 5-16a,b. SEM micrographs of ZAO thin film deposited on silicon wafer at an oxygen pressure of 0.14 mTorr. (a) Shows the ZAO thin film before degradation and (b) shows the variation between the degraded and non-degraded area.

## CHAPTER 6 CONCLUSIONS

The goal of this research was to use a novel modified pulsed laser ablation coating technique to apply a nano-meter scale coating to ZnS:Ag in an attempt to improve the phosphors cathodoluminescent (CL) lifetime. The nano-meter scale coatings were postulated to behave as a protective layer preventing electron beam stimulated surface chemical reactions from taking place, which attack the zinc in the phosphor to form a non-luminescent layer of ZnO.

Two grams of ZnS:Ag were coated with indium tin oxide (ITO) that was deposited at a pressure of  $5 \cdot 10^{-5}$  mTorr and subsequently degraded at  $6.1 \cdot 10^{-7}$  Torr and  $1 \cdot 10^{-7}$  Torr, which corresponds to a high and low level of water partial pressure, respectively. The resulting CL degradation curves showed that the amount of residual water vapor present during degradation had a dramatic effect on the rate of degradation. However, the application of the ITO coating to the ZnS:Ag slowed the CL degradation rate at both vacuum levels. In the higher partial pressure of water case, the coated phosphor maintained 70% of its initial brightness as compared to the uncoated phosphor, which only maintained 20% of its initial brightness at a coulomb dose of  $5 \text{ C/cm}^2$ . In the lower partial pressure of water case, the coated phosphor maintained 60% of its original brightness as compared to the uncoated phosphor, which only maintained 30% of its original brightness at a coulomb dose of  $25 \text{ C/cm}^2$ . Using x-ray photoelectron spectroscopy, the reduction in degradation rate due to the application of the ITO coating was shown to be the retardation of the chemical reactions between the reactive atomic

oxygen created from the electron beam surface stimulated chemical reactions and the zinc in ZnS:Ag. These results show that to obtain longer phosphor lifetimes, it is advantageous to not only have a nano-encapsulating ITO layer on the phosphor, but to also maintain a high vacuum level during electron beam irradiation with minimal water vapor present.

By coating ZnS:Ag with aluminum-doped zinc oxide (ZAO) at various oxygen deposition pressures, the effect of the coating properties on CL degradation was studied. In this research, three varying oxygen depositions were chosen. These three pressures provided ZAO films with three distinct properties: (1) high optical transmittance and low electrical conductivity (100 mTorr), (2) high optical transmittance and high electrical conductivity (0.6 mTorr), and (3) low optical transmittance and high electrical conductivity (0.14 mTorr). It was hypothesized that condition (2) would prevail to provide the longest CL lifetime. However, condition (3) where the ZAO film was deposited at the lowest oxygen deposition pressure (0.14 mTorr) provided the longest CL lifetime. These unexpected results showed that the electrical and optical properties of the ZAO coating were not the dominating factors in controlling the reduction of CL degradation. XPS was used to analyze the chemical changes in the properties of the ZAO coatings before and after degradation, while TEM was used to examine the coating uniformity. XPS showed that there was a large shift in the Zn 2p peak towards higher binding energies as compared to the other two coated samples. This indicated that the coating layer acted not only as a protective layer, but also as a scavenger or a getter material that reacts with the harmful dissociated atomic oxygen species to further oxidize the coating and in essence reduce the number of available harmful species. TEM showed

that the conformal coverage of the coated samples was much better for the 0.14 mTorr case than the 0.6 mTorr case. In the 0.14 mTorr case, TEM showed that ZnS:Ag had a continuous coating and was comprised of nanoclusters of approximately 10 nm in size. While in the 0.6 mTorr case, TEM revealed that the coating was discontinuous and was comprised of nanoclusters in the size range of 80-120 nm. This difference in coating coverage could be responsible for the variation in the CL degradation lifetimes between these two cases. Where the continuous coating provides better protection of the phosphor surface from the harmful residual gases, while the exposed areas of the non-continuous coating is more readily attacked by ESSCR and therefore degrades faster.

## LIST OF REFERENCES

- [Bad07] Badeker, K., *Ann. Phys.*, **22**, 749 (1907).
- [Bla94] Blasse, G. and Grabmaier, B.C., *Luminescent Materials*. Springer-Verlag, Berlin, Germany. (1994).
- [Bru92] Brundle, C.R., Evans, C.A. Jr., Wilson, S. *Encyclopedia of Materials Characterization*, Manning Publications, Greenwich, Conn. (1992).
- [Can02] Candescant, "Thin CRTs." Candescant, website, <http://www.candescant.com/Candescant/showcase.htm>; Jan. 30(2002).
- [Cap82] Caporaletti, O., *Solar Energy Mater.*, **7**, 65 (1982).
- [Cat95] Cathey, D.A. *Journal of SID*, **16** (1995).
- [Cha98] Chambers, A. *Basic Vacuum Technology*, Institute of Physics Publishing, Bristol, TN. (1998).
- [Cha01] Chang, J.F., Hon, M.H., *Thin Solid Films*, **386**, 79 (2001).
- [Che00] Chen, M., Pei, Z.L., Wang, X., Yu, Y.H., Liu, X.H., Sun, C., and Wen, L.S., *J. Appl. Phys. D: Appl. Phys. B* **33**, 2538 (2000).
- [Cho00] Chopra, K.L., Majo, S., and Pandya, D.K., *Thin Solid Films*, **102**, 1 (1983).
- [Cou00] Coutts, T.J., Young, D.L., Li, X., *MRS Bulletin*, **25** (8), 58 (2000).
- [Der92] Deroubaix, G. and Marcus, P., *Surf. Interf. Anal.*, **18**, 39 (1992).
- [Ell93] Ellmer, K., Kudella, F., Mientus, R., Schieck, R., and Fiechter, S., *Applied Surface Science*, **70/71**, 707 (1993).
- [Ell00] Ellmer, K., *J. Phys. D: Appl. Phys.*, **33**, R17 (2000).
- [Fut98] Futsuhara, M., Yoshioka, K., and Takai, O., *Thin Solid Films*, **322**, 274 (1998).
- [Gao00] Gao, H.J., Duschler, G., Kim, M., Pennycook, S.J., Kumar, D., Cho, K.G., and Singh, R.K., *Appl. Phys. Lett.*, **77**, 594 (2000).

- [Gil00] Gilkes, M.J., Nicolaescu, D., Wilshaw, P.R., *J. Vac. Sci. Technol. B*, **18** (2), 948 (2000).
- [Gol92] Goldstein, J.I., Newbury, D.E., Echlin, P., Joy, D.C., Romig, A.D., Jr., Lyman, C.E., Fiori, C., Lifshin, E. *Scanning Electron Microscopy and X-Ray Microanalysis*, Plenum Press, New York, New York. (1992).
- [Gor00] Gordon, R.G., *Mat. Res. Bull.*, **25** (8), 52 (2000).
- [Gra02] Granqvist, C.G., and Hultaker, A., *Thin Solid Films*, **411**, 1 (2002).
- [Gree01] Greeff, A.P. and Swart, H.C., *Surface and Interface Analysis*, **31**, 448 (2001).
- [Has90] Hase, T., Kano, T., Nakazawa, E., and Yamamoto, H., *Advances in Electronics and Electron Physics*, **79**, 271 (1990).
- [Hir97] Hiramatsu, M., Imaeda, K., Horio, N., and Nawata, M., *J. Vac. Sci. Technol. A*, **16** (2), 669 (1997).
- [Hol96] Holloway, P.H., Sebastian, J.S., Trottier, T., Jones, S., Swart, H., and Peterson, R.O., *Flat Panel Display Materials II, MRS Proceedings*, Pittsburgh, PA, 424. (1996).
- [Hol99] Holloway, P.H., Trottier, T.A., Abrams, B., Kondoleon, C., Jones, S.L., Sebastian, J.S., Thomes, W.J., and Swart, H., *J. Vac. Sci. Technol. B*, **17** (2), 752 (1999).
- [Hol00] Holloway, P.H., Trottier, T.A., Sebastian, J., Jones, S., Zhang, X.-M., Abrams, B., Thomes, W. J., and Kim, T.-J. *Journal of Applied Physics*, **88** (1), 483 (2000).
- [Hud92] Hudson, J.B. *Surface Science An Introduction*, Butterworth-Heinemann, Stoneham, MA. (1992).
- [Hum93] Hummel, R.E., *Electronic Properties of Materials*, Second Edition. Springer-Verlag, Berlin. Germany (1993).
- [Ito93] Itoh, S., Niiyama, T., and Yokoyama, M., *J. Vac. Sci. Technol. B*, **11** (3), 647 (1993).
- [Jar76] Jarzebski, Z.M., Marton, J.P., *J. Electrochem. Soc.*, **123** 199C, 299C, 333C (1976).
- [Jea00] Jean, J.H. and Yang, S.M., *J. Am. Ceram. Soc.*, **83** (8), 1928 (2000).
- [Jeo01] Jeong, W.J., and Park, G.C., *Solar Eng. Mat. And Solar Cells*, **65**, 37 (2001).
- [Joy89] Joy, D.C. and Luo, S., *Scanning*, **11**, 176 (1989).

- [Kaw00] Kawazoe, H., Yanagi, H., Ueda, K., and Hosono, H., *MRS Bulletin*, **25** (8), 28 (2000).
- [Kel97] Keller, P.A. *Information Display*, 12 (1997).
- [Kim00a] Kim, H., Gilmore, C.M., Horwitz, J.S., Pique, A., Murata, H., Kushto, G.P., Schlaf, R., Kafafi, Z.H., and Chrisey, D.B., *Amer. Ins. Phys.*, **76** (3), 259 (2000).
- [Kim00b] Kim, H, Pique, A., Horwitz, J.S., Murata, H., Kafafi, Z.H., Gilmore, C.M., and Chrisey, D.B., *Thin Solid Films*, **377-378**, 798 (2000).
- [Kom97] Kominami, H., Nakamura, T., Sowa, K., Nakanishi, Y., Hatanaka, Y., and Shimaoka, G., *App. Sur. Sci.*, **113/114**, 519 (1997).
- [Lak95] Lakshmikumar, S.T. and Rastogi, A.C., *Thin Solid Films* **259**, 150-153 (1995).
- [Lar02] Larimax. "Residual Gas Analysis – All You Need To Know." Larimax, website, [http://www.larimaxinstruments.com/new\\_page\\_6.htm](http://www.larimaxinstruments.com/new_page_6.htm); (2002).
- [Loo01] Look, D.C., *Mat. Sci. Eng. B*, **80**, 383 (2001).
- [Lew00] Lewis, B.G., and Paine, D.C., *Mat. Res. Bull.*, **25** (8), 22 (2000).
- [Mah99] Mahajan, S., and Sree Harsha, K.S., *Principles of Growth and Processing of Semiconductors*, McGraw-Hill, Boston, Massachusetts (1999).
- [Mal00] Malkomes, N. Vergohl, M., and szyszka, B., *J. Vac. Sci. Technol. A*, **19** (2), 414 (2000).
- [May90] Mayer, J.W., Lau, S.S., *Electronic Materials Science: For Integrated Circuits in Si and GaAs*. New York, NY. Macmillan Publishing Company. (1990).
- [Ohr92] Ohring, M., *The Materials Science of Thin Films*, San Diego. CA, Academic Press. (1992).
- [Oka79] Okada, A., Oka, T., *J. Appl. Phys.*, **50** (11), 6934 (1979).
- [Oos97] Oosthuizen, L., Swart, H.C., Viljoen, P.E., Holloway, P.H., Berning, G.L.P., *Appl. Sur. Sci.*, **120**, 9 (1997).
- [Rao74] Rao-Sahib, T.S. and Wittry, D.B., *J. Appl. Phys.*, **45** (11), 5060 (1974).
- [Reu00] Reuss, R.H. and Chalamala, B.R., *Mat. Res. Soc. Symp. Proc.*, **558**, 49 (2000).
- [Sch95] Schwoebel, P.R., and Brodie, I., *J. Vac. Sci. Technol. B*, **13** (4), 1391 (1995).
- [Sea97] Seager, C.H., Tallant, D.R., and Warren, W.L., *J. Appl. Phys.*, **82**, 4515 (1997).

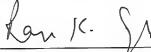
- [Sea01] Seager, C.H., Tallant, D.R., Shea, L., Zavaldil, K.R., Gnade, B., Holloway, P.H., Thomes, W.J., Abrams, B., Vecht, A., Gibbons, C.S., Trwoga, P., Summers, C.J., Wagner, B.K., and Penczek, J., *J. Appl. Sur. Sci.*, **161**, 1221 (2001).
- [Seb95] Sebastian, J., Jones, S., Trotter, T., Holloway, P. *Soc. Inf. Disp.*, **27** (4), 627 (1995).
- [Seb97] Sebastian, J.S., Ph.D. Dissertation, University of Florida, (1997).
- [Spi76] Spindt, C.A., Brodie, L., Pilione, L., Badzian, T., and Drawl, W., *J. Appl. Phys.*, **47**, 5248 (1976).
- [Swa96] Swart, H.C., Sebastian, J.S., Trotter, T.A., Jones, S.L., Holloway, P.H., *J. Vac. Sci. Technol. A*, **14** (3), 1697 (1996).
- [Swa99] Swart, H.C., Greeff, A.P., Holloway, P.H., Berning, G.L.P., *Appl. Sur. Sci.*, **140**, 63 (1999).
- [Swa00] Swart, H.C., Hillie, K.T., *Surface and Interface Analysis*, **30**, 383 (2000).
- [Tro96] Trotter, T.A., Swart, H.C., Jones, S.L., Sebastian, J.S., and Holloway, P.H., *J. Soc. Inf. Disp.*, **4**, 351 (1996).
- [Vil02] Villalobos, G.R., Bayya, S.S., Sanghera, J.S., and Miklos, R.E., *J. Am. Ceram. Soc.*, **85** (8), 2128 (2002).
- [Wan97] Wang, C.W., Sheu, T.J., Su, Y.K., and Yokoyama, M., *Appl. Surf. Sci.*, **113/114**, 709 (1997).
- [Wei98] Weiss, B.L., Badzian, A., Pilione, L., Badzian, T., Drawl, W., *J. Vac. Sci. Technol. B*, **16** (2), 681 (1998).
- [Yac90] Yacobi, B.G., and Holt, D.B., *Cathodoluminescence Microscopy of Inorganic Solids*, Plenum Press, New York, NY. (1990).



## BIOGRAPHICAL SKETCH

Michael Ollinger was born on December 8, 1973, in Spartanburg, South Carolina. He attended Spartanburg High School, where he graduated in 1992. The next five years were spent at Clemson University, where he graduated cum laude with a Bachelor of Science degree in Ceramic Engineering. Upon completion of his undergraduate degree in May of 1997, he spent the next five years at the University of Florida under the guidance of Dr. Rajiv Singh. He received his Master of Science degree in December of 2000.

I certify that I have read this study and that in my opinion it conforms to acceptable standards of scholarly presentation and is fully adequate, in scope and quality, as a dissertation for the degree of Doctor of Philosophy.



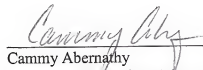
Rajiv K. Singh, Chairman  
Professor of Materials Science and  
Engineering

I certify that I have read this study and that in my opinion it conforms to acceptable standards of scholarly presentation and is fully adequate, in scope and quality, as a dissertation for the degree of Doctor of Philosophy.



Stephen J. Pearton  
Professor of Materials Science and  
Engineering

I certify that I have read this study and that in my opinion it conforms to acceptable standards of scholarly presentation and is fully adequate, in scope and quality, as a dissertation for the degree of Doctor of Philosophy.



Cammy Abernathy  
Professor of Materials Science and  
Engineering

I certify that I have read this study and that in my opinion it conforms to acceptable standards of scholarly presentation and is fully adequate, in scope and quality, as a dissertation for the degree of Doctor of Philosophy.



David P. Norton  
Associate Professor of Materials Science  
and Engineering

I certify that I have read this study and that in my opinion it conforms to acceptable standards of scholarly presentation and is fully adequate, in scope and quality, as a dissertation for the degree of Doctor of Philosophy.



---

Fan Ren  
Professor of Chemical Engineering

This dissertation was submitted to the Graduate Faculty of the College of Engineering and to the Graduate School and was accepted as partial fulfillment of the requirements for the degree of Doctor of Philosophy.

December 2002



---

Pramod P. Khargonekar  
Dean, College of Engineering

---

Winfred M. Phillips  
Dean, Graduate School

499F23<sup>T</sup>4673  
04/01/03 34768

